

# Gradient-based topology optimization of soft dielectrics as tunable phononic crystals

Atul Kumar Sharma<sup>a</sup>, Gal Shmuel<sup>b</sup>, Oded Amir<sup>c</sup>

<sup>a</sup>Department of Mechanical Engineering, Indian Institute of Technology Jodhpur, Jodhpur 342037, India

<sup>b</sup>Faculty of Mechanical Engineering, Technion–Israel Institute of Technology, Haifa 32000, Israel

<sup>c</sup>Faculty of Civil and Environmental Engineering, Technion–Israel Institute of Technology, Haifa 32000, Israel

---

## Abstract

Dielectric elastomers are active materials that undergo large deformations and change their instantaneous moduli when they are actuated by electric fields. By virtue of these features, composites made of soft dielectrics can filter waves across frequency bands that are *electrostatically tunable*. To date, to improve the performance of these adaptive phononic crystals, such as the width of these bands at the actuated state, metaheuristics-based topology optimization was used. However, the design freedom offered by this approach is limited because the number of function evaluations increases exponentially with the number of design variables. Here, we go beyond the limitations of this approach, by developing an efficient gradient-based topology optimization method. The numerical results of the method developed here demonstrate prohibited frequency bands that are indeed wider than those obtained from the previous metaheuristics-based method, while the computational cost to identify them is reduced by orders of magnitude.

**Keywords:** Dielectric elastomers, nonlinear electroelasticity, wave propagation, band gaps, composites, Bloch-Floquet waves, gradient-based topology optimization

---

## 1. Introduction

Dielectric elastomers (DEs) are active materials that undergo large deformations when they are actuated by electric fields (Pelrine et al., 2000; Hajiesmaili & Clarke, 2021). Moreover, the constitutive relations of DEs are nonlinear, such that their instantaneous moduli vary as functions of the electromechanical loads. These features have led to the design of various applications, such as haptic devices (Kim et al., 2016), soft robots (Gu et al., 2018), actuators (Hajiesmaili & Clarke, 2021; Sharma et al., 2018, 2019; Su et al., 2018, 2019; Ortigosa et al., 2021; Ortigosa & Martínez-Frutos, 2021) and artificial muscles (Lu et al., 2016), that are based on DEs.

More recently, the potential of DEs to function as adaptive waveguides has been explored (Zhu et al., 2020; Mohajer et al., 2021; Jandron & Henann, 2018; Ziser & Shmuel, 2017; Wang et al., 2020; Zhu et al., 2020). These studies are based on the understanding that the physical properties that govern elastic waves are electrostatically tunable. Following the pioneering work of Gei et al. (2011) on *flexural* waves, in a series of papers, Shmuel and collaborators (Shmuel & Debotton,

---

*Email addresses:* atulksharma@iitj.ac.in (Atul Kumar Sharma), meshmuel@technion.ac.il (Gal Shmuel), odedamir@technion.ac.il (Oded Amir)

14 2012; Shmuel, 2013; Shmuel & Pernas-Salomón, 2016; Getz et al., 2017; Getz & Shmuel, 2017;  
15 Bortot & Shmuel, 2017) have integrated this concept of material tunability with the theory of  
16 *acoustic* band structure, in order to design adaptive wave suppressors. Band theory predicts that  
17 waves in elastic composites (also termed phononic crystals) cannot propagate at certain frequencies  
18 (band gaps) owing to Bragg reflections, that are functions of the periodicity and the impedance  
19 mismatch of the phases (Kushwaha et al., 1993, 1994). The idea to tune these band gaps using DEs  
20 is simple: by applying a bias electromechanical field, the periodicity and impedance mismatch  
21 between the DE phases is tuned, which in turn change the Bragg reflections and the desired band  
22 gaps (Shmuel & Band, 2016; Lustig & Shmuel, 2018).

23 To achieve a significant tunability, these works have shown that large electric fields are needed—  
24 a requirement that hinders the practical utility of DEs as tunable phononic crystals. Since this  
25 tunability is a function of the microstructure of the composite, Bortot et al. (2018) have developed  
26 a scheme to identify unit cells that exhibit better performance based on *topology optimization*—a  
27 numerical method that systematically searches for optimal material distribution that under specified  
28 design and response constraints.

29 Research on topology optimization began with the seminal paper of Bendsøe & Kikuchi (1988)  
30 and recent advancements are discussed in several review articles (Sigmund & Maute, 2013; Deaton  
31 & Grandhi, 2014). For computational implementation, the design domain—a square unit cell in  
32 the current context—is discretized into a finite number of squares and a design variable is attached  
33 to each of their centroids. The value of the design variable then indicates which material is placed  
34 at the corresponding position in space. This allows for significant design freedom as there is no  
35 assumption regarding the topology of the unit cell. Consequently, vast improvement in performance  
36 can be achieved in comparison to unit cells of prescribed topology, e.g. a circular fiber within a  
37 surrounding matrix.

38 The use of topology optimization for maximizing phononic band gaps was pioneered by Sigmund  
39 & Søndergaard Jensen (2003). Their work was followed by many studies employing optimization  
40 techniques for synthesizing phononic crystals such that desired band gap characteristics are obtained  
41 (Halkjær & Jensen, 2006; Gazonas et al., 2006; Hussein et al., 2007; Bilal & Hussein, 2011; Liu  
42 et al., 2014, 2016; Li et al., 2016a; Xie et al., 2017; Lu et al., 2017; Xie et al., 2017; Yi et al.,  
43 2019; Liu et al., 2020; Quinteros et al., 2021; Zhang et al., 2021). Detailed reviews on topology  
44 optimization of phononic crystals were provided by Yi & Youn (2016) and Li et al. (2019).

45 The studies mentioned above aimed at optimizing the linear elastic response, while optimization  
46 techniques have been employed only recently for band gaps that depend on nonlinear elastic deformations  
47 (Hedayatrasa et al., 2016; Bortot et al., 2018; De Pascalis et al., 2020).

48 The limitation of these three studies, from the optimal design point of view, is that they are based  
49 on metaheuristics, specifically Genetic Algorithms (GA). These methods utilize only function  
50 evaluations and no gradient information is used to progress towards an optimum. Their main  
51 drawback is that the number of function evaluations that is needed increases exponentially with  
52 the number of design variables. Each evaluation consists of solving many generalized eigenvalue  
53 problems for generating the band diagram. This computational bottleneck limits the design resolution,  
54 i.e., the number of design variables that represent the material distribution, as can be seen in the  
55 respective results (Hedayatrasa et al., 2016; Bortot et al., 2018; De Pascalis et al., 2020).

56 The full potential of topology optimization can only be accessed if gradient-based optimization  
57 is used, so that the computational effort can be reduced by orders of magnitude and fine design  
58 resolution can be accommodated. Such efficient approach is developed here for the case study

59 considered by Bortot et al. (2018). The medium that they analyzed comprises soft dielectric fibers  
60 embedded periodically in a matrix made of a different deformable dielectric. The composite is  
61 quasistatically actuated by application of axial electric field. Under the assumption of incompressible  
62 phases, Shmuel (2013) has found a closed-form solution for the resultant deformation in terms of  
63 the bias electric field and the properties of the composite. Using a plane-wave expansion approach,  
64 Shmuel (2013) determined the band structure of incremental anti-plane waves propagating in the  
65 deformed configuration, the gaps of which were optimized by Bortot et al. (2018) using a GA  
66 method.

67 Here, we introduce a finite element formulation of the incremental problem, and use the properties  
68 of each element as the design variables, the objective of which is to maximize the width of the gap in  
69 the audible frequency range. In order to iteratively update the design variables, we employ gradient-  
70 based optimization, namely the Method of Moving Asymptotes—MMA (Svanberg, 1987). We  
71 carry out and implement fully analytical sensitivity analysis for computing the gradient of the  
72 objective function with respect to each one of the design variables. We generate optimized designs  
73 with superior performance compared to those obtained by Bortot et al. (2018), while the computational  
74 cost—in terms of the number of function evaluations—is smaller by orders of magnitude.

75 The paper is organized as follows. In Sec. 2 we provide the governing equations of electroelastic  
76 composites (Dorfmann & Ogden, 2005; Suo et al., 2008; Gei et al., 2013; DeBotton et al., 2007;  
77 Dorfmann & Ogden, 2010), upon which the forthcoming analysis is based. In Sec. 3 we recall the  
78 solution of Shmuel (2013) to the quasistatic deformation of the periodic DE composite owing to  
79 axial electric fields, and the equations developed therein for the incremental problem of anti-plane  
80 shear waves. In Sec. 4, we present our finite element formulation for the solution of the incremental  
81 problem, and specifically for the calculation of the band diagram of the deformed DE composite.  
82 The contribution of this work is detailed in Sec. 5 and Sec. 6, where we present the analytical design  
83 sensitivity analysis for computing the gradient of the objective function with respect to each one  
84 of the design variables; implement the method using in-house MatLab code; and present numerical  
85 examples. We conclude this paper with a summary of our results in Sec. 7.

## 86 2. Governing equations

87 In this section, we briefly summarize the governing equations pertaining to nonlinear electro-  
88 mechanical deformation of dielectric elastomers following the theory of nonlinear electroelasticity  
89 (Dorfmann & Ogden, 2005; Suo et al., 2008) and the associated linearized incremental theory  
90 (Dorfmann & Ogden, 2010).

### 91 2.1. Nonlinear electroelasticity theory

92 Consider an arbitrary deformable dielectric composite body  $\mathcal{B}^m \cup \mathcal{B}^f = \mathcal{B}$  made up of two  
93 incompressible homogeneous dielectric phases  $\mathcal{B}^m$  and  $\mathcal{B}^f$ , and surrounded by vacuum. In the  
94 undeformed configuration, the dielectric composite occupies a region  $\mathcal{B}_0^m \cup \mathcal{B}_0^f = \mathcal{B}_0$  with the  
95 boundary  $\partial\mathcal{B}_0$ . An arbitrary material particle in this configuration is denoted by its position vector  
96  $\mathbf{X}$ . When subjected to electromechanical loadings, the dielectric composite body is deformed and  
97 occupies a region  $\mathcal{B}_t^m \cup \mathcal{B}_t^f = \mathcal{B}_t$  with boundary  $\partial\mathcal{B}_t$ . The position of a material particle in the  
98 deformed configuration is denoted by  $\mathbf{x}$ , which is related to  $\mathbf{X}$  through the nonlinear deformation  
99 map  $\mathbf{x} = \boldsymbol{\chi}(\mathbf{X}, t)$ . The components of deformation gradient are given by  $F_{iJ} = \frac{\partial \chi_i(\mathbf{X}, t)}{\partial X_J}$ . The

100 determinant of the deformation gradient relates the volume ratio of an infinitesimal element in the  
 101 deformed state,  $dv$ , and its counterpart in the undeformed state,  $dV$ , such that  $J = \det(\mathbf{F}) > 0$ .  
 102 The components of the right Cauchy-green tensor are  $C_{IJ} = F_{iI}F_{iJ}$ .

For quasi-electrostatic processes, in the absence of free charges and currents, Gauss's law and Faraday's law are written as

$$\frac{\partial d_i}{\partial x_i} = 0, \quad \frac{\partial e_j}{\partial x_k} \epsilon_{ijk} = 0_i, \quad (1)$$

103 respectively, where  $\mathbf{d}$  and  $\mathbf{e}$  are the electric displacement and the electric field vectors in the  
 104 deformed configuration, respectively;  $\mathbf{0}$  represents the zero vector and  $\epsilon$  represents the Levi-Civita  
 105 symbol. In addition, the mechanical equilibrium equation in the deformed configuration, in the  
 106 absence of mechanical body forces, is

$$\frac{\partial \sigma_{ij}}{\partial x_j} = 0_i, \quad (2)$$

107 where  $\sigma$  is the symmetric *total* Cauchy stress tensor consisting of both mechanical and electrical  
 108 contributions.

109 In this paper, we consider infinite, periodic, dielectric composites, which possess internal, mechanical  
 110 traction and free charge interfaces between the two dielectric phases  $m$  and  $f$  with jump boundary  
 111 conditions

$$[[\sigma_{ij}]] n_j = 0_i, \quad [[d_i]] n_i = 0, \quad [[e_i]] n_j \epsilon_{ijk} = 0_k, \quad (3)$$

112 where  $[[\bullet]] = (\bullet)^m - (\bullet)^f$  represents the jump of quantities between the two phases, and  $\mathbf{n}$  represents  
 113 the unit normal vector on the deformed interface and directed from phase  $m$  to phase  $f$ .

In Lagrangian description that uses  $\mathbf{X}$  as the independent variable, the *total* first Piola-Kirchhoff stress tensor is related to the *total* Cauchy stress tensor by  $P_{iJ} = J\sigma_{ik}F_{kJ}^{-T}$  and satisfies the Lagrangian form of the equilibrium equation

$$\frac{\partial P_{iJ}}{\partial X_J} = 0_i, \quad (4)$$

in the undeformed configuration  $\mathcal{B}_0$ . The Lagrangian electric displacement and electric field are given as  $D_J = JF_{Ji}^{-1}d_i$  and  $E_J = F_{iJ}e_i$ , respectively. They satisfy the Lagrangian form of Gauss's law and Faraday's law

$$\frac{\partial D_J}{\partial X_J} = 0, \quad \frac{\partial E_J}{\partial X_K} \epsilon_{IJK} = 0_I, \quad (5)$$

114 respectively.

115 We consider non-dissipative materials for which the first Piola-Kirchhoff stress tensor  $\mathbf{P}$  and  
 116 Lagrangian electric field  $\mathbf{E}$  are obtained constitutively in terms of the deformation gradient  $\mathbf{F}$   
 117 and Lagrangian electric displacement  $\mathbf{D}$  through an *augmented* energy density function  $\psi(\mathbf{F}, \mathbf{D})$   
 118 as (Dorfmann & Ogden, 2005)

$$P_{iJ} = \frac{\partial \psi}{\partial F_{iJ}} - p_0 F_{iJ}^{-T}, \quad E_J = \frac{\partial \psi}{\partial D_J}, \quad (6)$$

119 where  $p_0$  is a Lagrange multiplier that accounts for the incompressibility constraint.

120 **2.2. The linearized incremental theory**

Following Dorfmann & Ogden (2010), we present the governing equations pertaining to the time dependent infinitesimal increment in both elastic and electric displacement fields  $\dot{\mathbf{x}} = \dot{\boldsymbol{\chi}}(\mathbf{X}, t)$ ,  $\dot{\mathbf{D}}(\mathbf{X}, t)$ , respectively, superimposed on the static deformed configuration characterized by the fields  $\boldsymbol{\chi}(\mathbf{X}, t)$  and  $\mathbf{D}(\mathbf{X}, t)$ . Henceforth, the infinitesimal incremental quantities are denoted with the superposed dot. The *push-forwards* of increments in the *total* first Piola–Kirchhoff stress, the Lagrangian electric displacement and the Lagrangian electric fields are

$$\Sigma_{ij} = \frac{1}{J} \dot{P}_{iK} F_{jK}, \quad \check{d}_i = \frac{1}{J} F_{iJ} \dot{D}_J, \quad \check{e}_i = F_{Ji}^{-1} \dot{E}_J, \quad (7)$$

121 respectively, satisfying the incremental forms of Gauss’s, Faraday’s laws, and momentum balance  
122 equation,

$$\frac{\partial \check{d}_i}{\partial x_i} = 0, \quad \frac{\partial \check{e}_j}{\partial x_k} \epsilon_{ijk} = 0_i, \quad \frac{\partial \Sigma_{ij}}{\partial x_j} = \rho \frac{\partial^2 \dot{x}_i}{\partial t^2}, \quad (8)$$

123 respectively, where  $\dot{\mathbf{x}}(\mathbf{x}, t) := \dot{\boldsymbol{\chi}}(\mathbf{X}, t)$ .

124 For an incompressible dielectric elastomer material, the linearized incremental constitutive laws  
125 in terms of the increments  $\Sigma$  and  $\check{e}$  are obtained using Eq. (6) and the push-forward operation as

$$\begin{aligned} \Sigma_{ij} &= \mathcal{C}_{ijkl} h_{kl} + p_0 h_{ji} - \dot{p}_0 \delta_{ij} + \mathcal{B}_{ijk} \check{d}_k, \\ \check{e}_i &= \mathcal{B}_{lki} h_{kl} + \mathcal{A}_{ij} \check{d}_j, \end{aligned} \quad (9)$$

where

$$\begin{aligned} \mathcal{C}_{ijkl} &= \frac{1}{J} F_{jI} \frac{\partial^2 \psi}{\partial F_{iJ} \partial F_{kJ}} F_{lJ}, & \mathcal{B}_{ijk} &= F_{jI} \frac{\partial^2 \psi}{\partial F_{iI} \partial D_J} F_{Jk}^{-1}, \\ \mathcal{A}_{ij} &= J F_{Ii}^{-1} \frac{\partial^2 \psi}{\partial D_I \partial D_J} F_{Jj}^{-1}, \end{aligned} \quad (10)$$

126 are the spatial constitutive tangent moduli, and  $h_{ij} = \frac{\partial \dot{x}_i}{\partial x_j}$  is subjected to incompressibility constraint  
127  $h_{kk} = 0$ .

128 **3. Quasistatic finite deformation and incremental anti-plane shear waves in DE composites**

129 As mentioned, using the above theory, Shmuel (2013) determined the quasistatic deformation  
130 of the periodic DE composite owing to axial electric fields [see also the study by Sharma et al.  
131 (2021)], and developed the equations that govern incremental anti-plane shear waves propagating  
132 through the deformed composite. For the convenience of the reader, we briefly summarize next the  
133 quasistatic solution and incremental equations, to which we will develop a finite element solution  
134 and develop the optimization process.

135 We consider a dielectric elastomer composite that is infinitely periodic in the  $(x_1, x_2)$  plane. The  
136 composite is made of incompressible DE fibers along the  $x_3$  direction with arbitrary cross-section  
137 (phase  $f$ ), that are embedded in a different incompressible DE matrix (phase  $m$ ). The constitutive  
138 response of the phases is given by the augmented Gentian free energy density function (Zhao et al.,

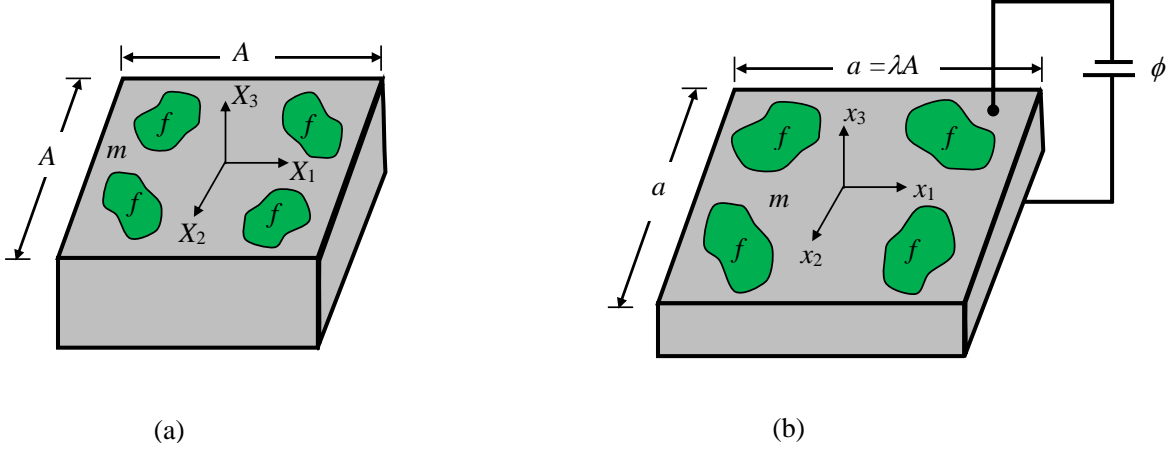


Figure 1: Dielectric elastomer fiber composite in the (a) undeformed configuration, and (b) deformed configuration, when subjected to an axial electric field.

139 2007; Sharma, 2020):

$$\psi(F_{iJ}, D_P) = -\frac{\mu J_m}{2} \ln \left[ 1 - \frac{F_{iJ} F_{iJ} - 3}{J_m} \right] + \frac{1}{2\varepsilon} D_P F_{iP} F_{iQ} D_Q, \quad (11)$$

where  $\varepsilon$  is the dielectric permittivity,  $\mu$  is the shear modulus of the dielectric elastomer,  $J_m$  is a dimensionless material parameter that accounts for the strain stiffening that arises from the limited extensibility of the elastomers. Figure 1a shows the schematic of a square DE composite unit cell of length  $A$  in the undeformed configuration. The composite is subjected to an average electric field of magnitude  $e_3$  in the  $x_3$  direction, and is free to expand in the transverse  $(x_1, x_2)$  plane. Shmuel (2013) has shown that the resultant deformation and electric field are homogeneous, in the form

$$\mathbf{F}^{(m)} = \mathbf{F}^{(f)} = \begin{bmatrix} \lambda & 0 & 0 \\ 0 & \lambda & 0 \\ 0 & 0 & \lambda^{-2} \end{bmatrix}, \quad \mathbf{e}^{(m)} = \mathbf{e}^{(f)} = \begin{bmatrix} 0 \\ 0 \\ e_3 \end{bmatrix}, \quad (12)$$

140 where the in-plane stretch ratio  $\lambda$  is given by the solution of the nonlinear equation

$$\bar{\mu} (\lambda^2 - \lambda^{-4}) = \bar{\varepsilon} e_3^2, \quad (13)$$

141 where  $\check{\mu}^{(p)} = \frac{\mu^{(p)} J_m^{(p)}}{J_m^{(p)} - 2\lambda^2 - \lambda^{-4} + 3}$ ,  $(\bar{\bullet}) = v^{(m)}(\bullet) + v^{(f)}(\bullet)$  and  $v^{(p)}$  is the volume fraction of  
 142 phase  $p$ . Thus, up to the point of bifurcation, for any given value of applied electric field  $e_3$  and  
 143 properties of the composite, the solution of Eq. (13) delivers the resultant deformation.

144 On the top of deformed configuration, we consider anti-plane waves propagating in the  $(x_1, x_2)$   
 145 plane of the composite. Figure 2a shows the schematic of the DE fiber composite unit cell in the  
 146 deformed  $(x_1, x_2)$  plane. Let  $\dot{x}_3(\mathbf{x}, t)$  and  $\dot{\phi}(\mathbf{x}, t)$  denote the anti-plane incremental displacement  
 147 and the incremental electric potential, respectively; the equations that govern these two unknown

148 fields are

$$\frac{\partial}{\partial x_j} \left( \tilde{\mu}(\mathbf{x}) \frac{\partial \dot{x}_3(\mathbf{x}, t)}{\partial x_j} - \tilde{d}(\mathbf{x}) \frac{\partial \dot{\phi}(\mathbf{x}, t)}{\partial x_j} \right) = \rho(\mathbf{x}) \frac{\partial^2 \dot{x}_3}{\partial t^2}, \quad (14)$$

$$\frac{\partial}{\partial x_j} \left( -\tilde{d}(\mathbf{x}) \frac{\partial \dot{x}_3(\mathbf{x}, t)}{\partial x_j} - \varepsilon(\mathbf{x}) \frac{\partial \dot{\phi}(\mathbf{x}, t)}{\partial x_j} \right) = 0, \quad (15)$$

149 respectively, where  $j = 1, 2$ ,  $\tilde{\mu}(\mathbf{x}) = \check{\mu}(\mathbf{x})\lambda^2 - \varepsilon(\mathbf{x})e_3^2$ , and  $\tilde{d}(\mathbf{x}) = \varepsilon(\mathbf{x})e_3$ .

150 Eqs. (14)-(15) are the starting point of our analysis: in the next Sec. we develop a finite element  
 151 formulation to solve them, and in turn obtain the band diagram of incremental anti-plane shear  
 152 waves in the DE composite. Based on the finite element formulation, we will develop Later a  
 153 gradient-based topology optimization method, the objective of which is to identify optimal unit-  
 154 cells that generate the widest band gaps at designated electric fields.

#### 155 4. Finite element formulation

156 We introduce next a finite element formulation with Bloch-Floquet periodic boundary conditions  
 157 (Kittel et al., 1996) to solve Eqs. (14)-(15). With  $\delta \dot{x}_3$  and  $\delta \dot{\phi}$  denoting virtual incremental anti-plane  
 158 displacement and virtual incremental electric potential, respectively, the weak form statements  
 159 corresponding to Eq. (14) and Eq. (15) are written as

$$\int_{\mathcal{B}_t} \left( \tilde{\mu} \frac{\partial \dot{x}_3}{\partial x_j} - \tilde{d} \frac{\partial \dot{\phi}}{\partial x_j} \right) \frac{\partial \delta \dot{x}_3}{\partial x_j} ds = \int_{\mathcal{B}_t} \rho \delta \dot{x}_3 \frac{\partial^2 \dot{x}_3}{\partial t^2} ds, \quad (16)$$

$$\int_{\mathcal{B}_t} \left( -\tilde{d} \frac{\partial \dot{x}_3}{\partial x_j} - \varepsilon \frac{\partial \dot{\phi}}{\partial x_j} \right) \frac{\partial \delta \dot{\phi}}{\partial x_j} ds = 0, \quad (17)$$

160 respectively, where  $s$  is the area of the unit cell in the deformed configuration.

161 The DE composite unit cell is discretized using finite elements,  $\mathcal{B}_t = \cup \mathcal{B}_t^e$ , and finite element  
 162 approximation for the incremental displacement and electric potential fields inside the element  $\mathcal{B}_t^e$   
 163 are written using the Voigt notation as

$$\dot{x}_3 = N_a \dot{x}_{a3}; \quad \dot{\phi} = N_a \dot{\phi}_a, \quad (18)$$

164 where  $N_a$  represents the shape function associated with node  $a$  of the element, and  $\dot{x}_{a3}$  and  $\dot{\phi}_a$   
 165 are the incremental anti-plane displacement and the incremental electric potential values at node  
 166  $a$ . Substituting above finite approximations and the linearized constitutive relations of Eq. (9) into  
 167 Eqs. (16)-(17), the elemental level equations corresponding to momentum balance and Gauss law  
 168 are written as

$$[K^{mm}] \{ \dot{x}_{b3} \} + [K^{me}] \{ \dot{\phi}_b \} = [M] \left\{ \frac{\partial^2 \dot{x}_{b3}}{\partial t^2} \right\}, \quad (19)$$

$$[K^{em}] \{ \dot{x}_{b3} \} + [K^{ee}] \{ \dot{\phi}_b \} = 0, \quad (20)$$

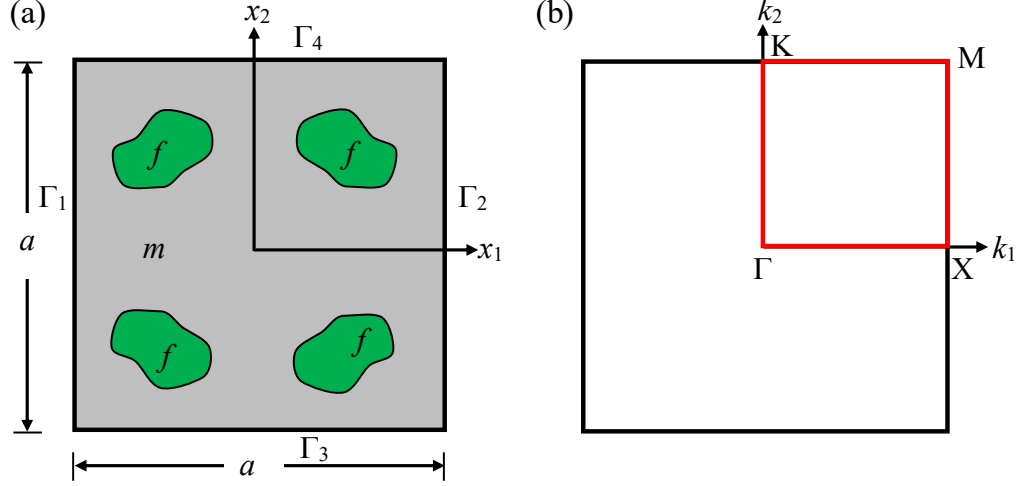


Figure 2: (a) Schematic description of the twice-symmetric square unit cell in the periodicity plane  $(x_1, x_2)$ , and (b) the corresponding first Brillouin zone with line segments to be scanned for determining the gaps extrema.

169 where  $K^{mm}$  is the mechanical stiffness matrix,  $K^{me}$  and  $K^{em}$  are the electro-mechanical coupled  
 170 stiffness matrices,  $K^{ee}$  is the electric stiffness matrix, and  $M$  is the mass matrix. The expressions  
 171 for these elemental stiffness matrices are given as

$$K^{mm} = \int_{B_t^e} \tilde{\mu} \frac{\partial N_a}{\partial x_j} \frac{\partial N_b}{\partial x_j} ds, \quad (21)$$

$$K^{me} = - \int_{B_t^e} \tilde{d} \frac{\partial N_a}{\partial x_j} \frac{\partial N_b}{\partial x_j} ds, \quad (22)$$

$$K^{em} = - \int_{B_t^e} \tilde{d} \frac{\partial N_a}{\partial x_j} \frac{\partial N_b}{\partial x_j} ds, \quad (23)$$

$$K^{ee} = - \int_{B_t^e} \varepsilon \frac{\partial N_a}{\partial x_j} \frac{\partial N_b}{\partial x_j} ds, \quad (24)$$

$$M = \int_{B_t^e} \rho N_a N_b ds. \quad (25)$$

172 Further, by assuming both the nodal incremental displacement and the incremental electric  
 173 potential to be time harmonic as

$$\dot{x}_{b3} = \tilde{x}_b(x) e^{-i\omega t}; \quad \dot{\phi}_b = \tilde{\phi}_b(x) e^{-i\omega t}, \quad (26)$$

174 and inserting these harmonic expressions into Eqs. (19)-(20), we get the incremental elemental

175 level equations governing the electro-elastic wave motion with angular frequency  $\omega$  as

$$[K^{mm}] \{\tilde{x}_b\} + [K^{me}] \{\tilde{\phi}_b\} - \omega^2 [M] \{\tilde{x}_b\} = 0, \quad (27)$$

$$[K^{em}] \{\tilde{x}_b\} + [K^{ee}] \{\tilde{\phi}_b\} = 0, \quad (28)$$

176 where  $\tilde{x}_b$  and  $\tilde{\phi}_b$  denote the spatially dependent nodal incremental displacement and electric potential  
 177 fields, respectively. Eliminating  $\tilde{\phi}_b$  from Eq. (27) by substituting  $\{\tilde{\phi}_b\} = -[G][K^{em}]\{\tilde{x}_b\}$  from  
 178 Eq. (28), we finally obtain the following eigenvalue problem

$$\begin{aligned} & ([K^{mm} - K^{me}GK^{em}] - \omega^2 [M]) \{\tilde{x}_b\} \\ & = ([K^*] - \omega^2 [M]) \{\tilde{x}_b\} = 0, \end{aligned} \quad (29)$$

179 where  $K^* = K^{mm} - K^{me}GK^{em}$  and  $G$  denotes the Moore–Penrose pseudoinverse of the electric  
 180 stiffness matrix  $K^{ee}$ .

181 Using the Bloch theorem (Kittel et al., 1996), we specify the periodic boundary conditions for  
 182 analyzing the anti-plane wave propagation through the infinite, periodic DE composite. For the DE  
 183 composite with square lattice shown in Fig. 2a, the Bloch periodic boundary conditions for the  
 184 nodal displacements are expressed as (Vatanabe et al., 2014; Jandron & Henann, 2018)

$$\begin{aligned} \tilde{x}_b(x_{\Gamma_2}) &= \exp(ik_1a)\tilde{x}_b(x_{\Gamma_1}), \\ \tilde{x}_b(x_{\Gamma_4}) &= \exp(ik_2a)\tilde{x}_b(x_{\Gamma_3}). \end{aligned} \quad (30)$$

185 Similarly, the Bloch periodic boundary conditions for the nodal electric potential fields are expressed  
 186 as

$$\begin{aligned} \tilde{\phi}_b(x_{\Gamma_2}) &= \exp(ik_1a)\tilde{\phi}_b(x_{\Gamma_1}), \\ \tilde{\phi}_b(x_{\Gamma_4}) &= \exp(ik_2a)\tilde{\phi}_b(x_{\Gamma_3}), \end{aligned} \quad (31)$$

187 where  $k_1$  and  $k_2$  are the component of real Bloch wave vector  $\mathbf{k} = k_i e_i$  along  $x_1$  and  $x_2$  directions,  
 188 as shown in Fig. 2b. In order to implement these complex-valued boundary conditions, we used  
 189 the augmented penalty method (Felippa, 2001; Oliveira et al., 2010).

190 The eigenvalue problem stated in Eq. (29) along with the Bloch periodic boundary conditions  
 191 of Eqs. (30)-(31) is solved for computing the band diagram, i.e,  $\omega$  as a function of the wave vector  
 192  $\mathbf{k}$ . Due to the quarter symmetry of the problem considered in this paper (see Fig. 2a), it is sufficient  
 193 to consider only the wave vector along the edges  $[\Gamma - X - M - K - \Gamma]$  of the first Brillouin  
 194 zone, marked by red lines in Fig. 2b (Sigmund & Søndergaard Jensen, 2003; Vatanabe et al., 2014;  
 195 Meng et al., 2017; Yi & Youn, 2016). The coordinates of various points along these edges are as  
 196  $\Gamma = (0, 0)$ ,  $X = (\pi/a, 0)$ ,  $M = (\pi/a, \pi/a)$ , and  $K = (0, \pi/a)$ .

197 Having at hand a finite-element formulation to calculate the band diagram, we proceed next to  
 198 develop the gradient-based topology optimization method, whose aim is to find the microstructure  
 199 that results with the widest band gaps at prescribed electric fields.

## 200 5. Topology optimization

201 In the design of phononic band gap structures, we need to find the unit cell that yields the  
 202 desired band gap characteristics. In this section, we introduce the topology optimization method

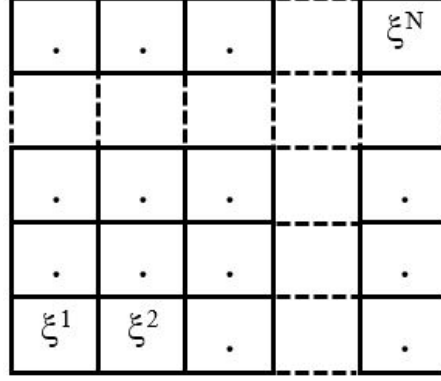


Figure 3: Discretization of the unit cell into  $N$  finite elements and assignment of a design variable to each finite element.

203 for obtaining the optimized distribution of the matrix and fiber phases in the DE composite unit cell  
 204 that maximizes the band gap size.

### 205 5.1. Material property interpolation for topology optimization

206 In this work, the design domain is a unit cell that is discretized by finite elements. To interpolate  
 207 the material properties for each finite element used to discretize the design domain, artificial design  
 208 variables  $\xi^e \in [0, 1]$  ( $e = 1, 2, \dots, N$ ,  $N$  being the total number of finite elements in the design  
 209 domain) are assigned to all finite elements as shown in Fig. 3.

210 For example,  $\xi^e = 0$  represents an element  $e$  that is composed of matrix phase, while  $\xi^e = 1$   
 211 represents an element consisting of fiber phase. As discussed by Sigmund & Søndergaard Jensen  
 212 (2003) and Meng et al. (2017), the material properties for each finite element in the design domain  
 213 can be interpolated linearly between the matrix and fiber phases as

$$\rho^e = (1 - \xi^e)\rho^{(m)} + \xi^e\rho^{(f)}, \quad (32)$$

$$\mu^e = (1 - \xi^e)\mu^{(m)} + \xi^e\mu^{(f)}, \quad (33)$$

$$\varepsilon^e = (1 - \xi^e)\varepsilon^{(m)} + \xi^e\varepsilon^{(f)}, \quad (34)$$

$$J_m^e = (1 - \xi^e)J_m^{(m)} + \xi^e J_m^{(f)}. \quad (35)$$

### 214 5.2. Optimization problem

The topology optimization problem aims to maximize the band gap width between the two adjacent bands in the audible frequency range 0-10 kHz. For two adjacent bands, assuming the eigenfrequencies corresponding to overlying band and underlying band to be  $\omega_{j+1}$  and  $\omega_j$ , respectively,

the objective function may be written as

$$f = \begin{cases} 10\text{kHz} - \max \omega_j(\xi, \mathbf{k})/2\pi \\ \quad \text{if } \min \omega_{j+1}(\xi, \mathbf{k})/2\pi \geq 10\text{kHz}, \\ (\min \omega_{j+1}(\xi, \mathbf{k}) - \max \omega_j(\xi, \mathbf{k}))/2\pi \\ \quad \text{if } \min \omega_{j+1}(\xi, \mathbf{k})/2\pi \leq 10\text{kHz}, \end{cases} \quad (36)$$

where,  $\max \omega_j(\xi, \mathbf{k})$  and  $\min \omega_j(\xi, \mathbf{k})$  represent the maximum and minimum of the  $j^{\text{th}}$  eigenfrequency  $\omega_j$ , respectively, over the  $\mathbf{k}$  vector for a given design of the unit cell domain,  $\xi$ .

We note that this objective function is not strictly differentiable because the location of maximum and minimum eigenvalues over the  $\mathbf{k}$ -vector may change from one design iteration to another. The problem can be regularized using smooth maximum and minimum functions, as described in the appendix. The results we achieved with the smooth formulation are essentially identical to those achieved with the objective of Eq. (36) and therefore we limit the discussion to a brief comparison in the appendix. It should be noted that in most gradient-based topology optimization studies on band gaps, the issue of differentiability is not discussed and we presume that the results reported in the literature were obtained with standard maximum and minimum operators. One exception we found is the work of Qian & Sigmund (2011) where a smooth bound formulation is employed.

The topology optimization problem may be stated as

$$\begin{aligned} \max_{\xi} \quad & f \\ \text{s.t. :} \quad & (K^*(\mathbf{k}) - \omega^2 M) \tilde{x}_b = 0, \quad \mathbf{k} \in [\Gamma - X - M - K - \Gamma] \\ & 0 \leq \xi_e \leq 1, \quad e = 1, \dots, N. \end{aligned} \quad (37)$$

### 5.3. Design sensitivity analysis

In order to iteratively update the design variables, we utilize gradient-based optimization, specifically MMA (Svanberg, 1987). This requires the evaluation of the gradient of the objective function with respect to any individual design variable,  $\xi^e$ . The derivative of the objective function  $f$  in Eq. (36) with respect to the design variable  $\xi^e$  is obtained as

$$\frac{\partial f}{\partial \xi^e} = \begin{cases} -\frac{1}{2\pi} \frac{\partial (\max \omega_n(\xi, \mathbf{k}))}{\partial \xi^e}, & \text{if } \min \omega_{n+1}(\xi, \mathbf{k})/2\pi \geq 10\text{kHz}; \\ \frac{1}{2\pi} \left( \frac{\partial (\min \omega_{n+1}(\xi, \mathbf{k}))}{\partial \xi^e} - \frac{\partial (\max \omega_n(\xi, \mathbf{k}))}{\partial \xi^e} \right), & \text{if } \min \omega_{n+1}(\xi, \mathbf{k})/2\pi \leq 10\text{kHz}. \end{cases} \quad (38)$$

For evaluating the objective function derivative in Eq. (38), the derivative of the eigenfrequency with respect to the design variable must be evaluated. For a given wave vector  $\mathbf{k}$ , the derivative of an eigenfrequency  $\omega_n$  with respect to the design variable is computed by differentiating Eq. (29) with respect to the design variable  $\xi^e$ , as follows

$$\frac{\partial (\omega_n(\xi, \mathbf{k}))}{\partial \xi^e} = \frac{1}{2\omega_n} \tilde{x}_b^{*T} \left( \frac{\partial K^*(\mathbf{k})}{\partial \xi^e} - \omega_n^2 \frac{\partial M}{\partial \xi^e} \right) \tilde{x}_b^*, \quad (39)$$

236 where,  $\tilde{x}_b^*$  is the global mass normalized eigenvector, and the derivative of the condensed stiffness  
 237 matrix  $K^*$  with respect to the design variable is obtained as

$$\begin{aligned} \frac{\partial K^*}{\partial \xi^e} = & \frac{\partial K^{mm}}{\partial \xi^e} - \frac{\partial K^{me}}{\partial \xi^e} (K^{ee})^{-1} K^{em} + \\ & K^{me} (K^{ee})^{-2} K^{em} \frac{\partial K^{ee}}{\partial \xi^e} - K^{me} (K^{ee})^{-1} \frac{\partial K^{em}}{\partial \xi^e}. \end{aligned} \quad (40)$$

238 The derivatives of the stiffness and the mass matrices  $\frac{\partial K^{mm}}{\partial \xi^e}$ ,  $\frac{\partial K^{me}}{\partial \xi^e}$ ,  $\frac{\partial K^{em}}{\partial \xi^e}$ ,  $\frac{\partial K^{ee}}{\partial \xi^e}$ , and  $\frac{\partial M}{\partial \xi^e}$   
 239 in Eqs. (39)-(40), are evaluated using Eqs. (21)-(25) as follows

$$\frac{\partial K^{mm}}{\partial \xi^e} = \int_{\mathcal{B}_t^e} \frac{\partial \tilde{\mu}^e}{\partial \xi^e} \frac{\partial N_a}{\partial x_j} \frac{\partial N_b}{\partial x_j} ds, \quad (41)$$

$$\frac{\partial K^{me}}{\partial \xi^e} = - \int_{\mathcal{B}_t^e} \frac{\partial \tilde{d}^e}{\partial \xi^e} \frac{\partial N_a}{\partial x_j} \frac{\partial N_b}{\partial x_j} ds, \quad (42)$$

$$\frac{\partial K^{em}}{\partial \xi^e} = - \int_{\mathcal{B}_t^e} \frac{\partial \tilde{d}^e}{\partial \xi^e} \frac{\partial N_a}{\partial x_j} \frac{\partial N_b}{\partial x_j} ds, \quad (43)$$

$$\frac{\partial K^{ee}}{\partial \xi^e} = - \int_{\mathcal{B}_t^e} \frac{\partial \varepsilon^e}{\partial \xi^e} \frac{\partial N_a}{\partial x_j} \frac{\partial N_b}{\partial x_j} ds, \quad (44)$$

$$\frac{\partial M}{\partial \xi^e} = \int_{\mathcal{B}_t^e} \frac{\partial \rho^e}{\partial \xi^e} N_a N_b ds, \quad (45)$$

240 in which the calculation of the derivatives of material parameters  $\rho^e$ ,  $\varepsilon^e$  and  $\tilde{d}^e$  with regard to  $\xi_e$  is  
 241 straightforward from Eqs. (32) and (34):  $\frac{\partial \rho^e}{\partial \xi^e} = \rho^{(f)} - \rho^{(m)}$ ,  $\frac{\partial \varepsilon^e}{\partial \xi^e} = \varepsilon^{(f)} - \varepsilon^{(m)}$ , and  $\frac{\partial \tilde{d}^e}{\partial \xi^e} = e_3 \frac{\partial \varepsilon^e}{\partial \xi^e}$ ,  
 242 while the evaluation of the derivative of  $\tilde{\mu}^e$  with regard to  $\xi_e$  is more involved, as follows

$$\begin{aligned} \frac{\partial \tilde{\mu}^e}{\partial \xi^e} = & \frac{\left[ 2\mu^e J_m^e \lambda \frac{\partial \lambda}{\partial \xi^e} + \lambda^2 \left( \mu^e \frac{\partial J_m^e}{\partial \xi^e} + \frac{\partial \mu^e}{\partial \xi^e} J_m^e \right) \right]}{(J_m^e - 2\lambda^2 - \lambda^{-4} + 3)} - \\ & \frac{\mu J_m^e \lambda^2 \left[ \frac{\partial J_m^e}{\partial \xi^e} - 4\lambda \frac{\partial \lambda}{\partial \xi^e} + 4\lambda^{-5} \frac{\partial \lambda}{\partial \xi^e} \right]}{(J_m^e - 2\lambda^2 - \lambda^{-4} + 3)^2} - \frac{\partial \varepsilon^e}{\partial \xi^e} e_3^2, \end{aligned} \quad (46)$$

243 where  $\frac{\partial J_m^e}{\partial \xi^e} = J_m^{(f)} - J_m^{(m)}$ , and the derivative of the stretch parameter with respect of design

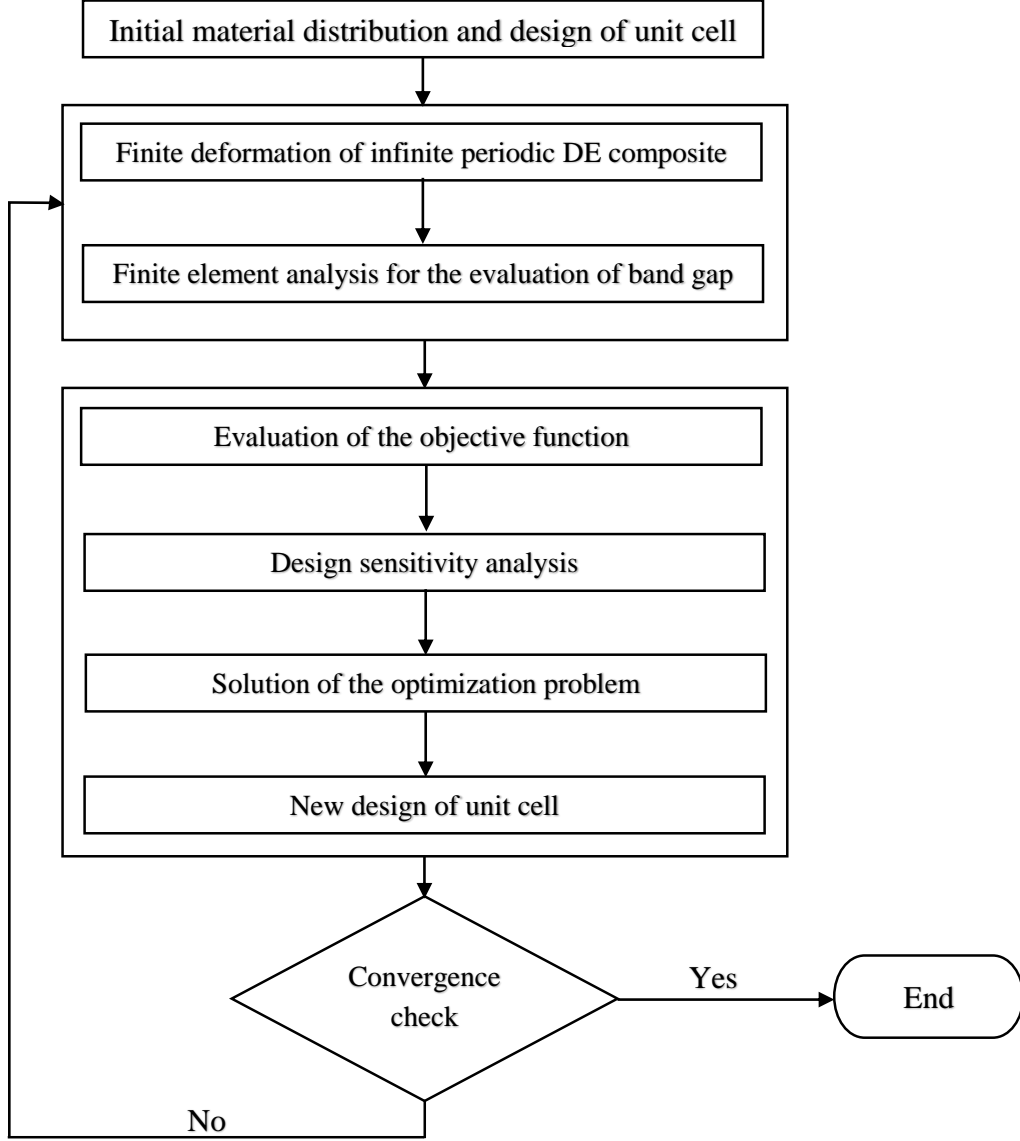


Figure 4: A schematic representation of the optimization process.

244 variable  $\frac{\partial \lambda}{\partial \xi^e}$  is evaluated by differentiating Eq. (13) with respect to  $\xi^e$  and expressed as

$$\frac{\partial \lambda}{\partial \xi^e} = \frac{\left[ (\varepsilon^{(f)} - \varepsilon^{(m)}) e_3^2 - (\lambda^2 - \lambda^{-4}) \left( \frac{\mu^e (J_m^{(f)} - J_m^{(m)}) + J_m^e (\mu^{(f)} - \mu^{(m)})}{(J_m^e - 2\lambda^2 - \lambda^{-4} + 3)} + \frac{\mu^e J_m^e (J_m^{(f)} - J_m^{(m)})}{(J_m^e - 2\lambda^2 - \lambda^{-4} + 3)^2} \right) \right]}{\left[ (2\lambda^2 + 4\lambda^{-5}) \left( \sum_{e=1}^N \mu^e \right) + (\lambda^2 - \lambda^{-4}) (4\lambda - 4\lambda^{-5}) \left( \sum_{e=1}^N \frac{\mu^e J_m^e}{(J_m^e - 2\lambda^2 - \lambda^{-4} + 3)^2} \right) \right]} \quad (47)$$

245 Finally, we note that the design derivatives computed according on the analytical expressions  
 246 herein were found to be in perfect agreement with numerical derivatives using finite differences,

Table 1: Material properties.

	Material	
	Silicone CF19-2186	Polyurethane PT6100S
Shear modulus $\mu$ (kPa)	333	5667
Locking parameter $J_m$	46.3	6.67
Relative permittivity $\epsilon_r$	2.8	7
Density $\rho$ (kg/m <sup>3</sup> )	1100	1200

247 hence the correctness of our derivations is verified.

#### 248 5.4. Implementation

249 The topology optimization framework presented in this paper is implemented by developing  
 250 an in-house MATLAB code. The topology optimization process starts with generating one quarter  
 251 of a twice-symmetric structure of the unit cell. In order to generate a symmetric unit cell, we  
 252 randomly distribute design variables in one quarter of the unit cell, and assign these design variables  
 253 symmetrically in the other three quarters. We note that this initial unit cell structure may not have  
 254 gaps in its spectrum. Then, based on the finite element framework introduced in Section 3, we  
 255 obtain the band diagram and the corresponding eigenvectors. Accordingly, the objective function  
 256 is evaluated. Subsequently, we evaluate the gradient of the objective with respect to the design  
 257 variables using Eq. (38). According to the evaluated objective function gradients, MMA proposes  
 258 a new vector of design variables by solving a convex subproblem. This yields the formation of a  
 259 new structure with the updated design variables. Thereafter, we repeat the finite element analysis  
 260 for the evaluation of band gaps and MMA optimization scheme for updating the design variables.  
 261 Such an iterative process continues until the maximum change in any design variable is less than  
 262  $10^{-6}$ . Figure 4 depicts schematic representation of the iterative optimization process.

### 263 6. Numerical results and discussions

264 In this section, we provide the numerical results for the phononic band gaps in dielectric  
 265 elastomers designed by using the topology optimization framework presented in the previous section.  
 266 The dielectric elastomer composite is assumed to be composed of polyurethane PT6100S fibers  
 267 embedded in the silicone CF19-2186 matrix (Getz et al., 2017). The properties of these materials  
 268 are listed in Table 1. In the undeformed configuration, we set the lattice parameter or the size of  
 269 the square unit cell to be  $A = 6.3$  mm. In order to discretize the unit cell, we used the four nodes,  
 270 linear quadrilateral finite elements with two degrees of freedom (one anti-plane displacement and  
 271 one electric potential) per node.

#### 272 6.1. Validation of the finite element framework

273 First, for validating the finite element framework presented in Section 4 and investigating the  
 274 influence of the bias electric field on the band structure, we compute the performance of a standard  
 275 unit cell composed of circular fibers embedded in the matrix, as shown in Fig. 5a. The volume  
 276 fraction of fibers in the unit cell is taken to be 0.5. The unit cell is discretized by 1139 quadrilateral  
 277 finite elements as shown in Fig. 5a (left). In all the plots in this paper, the yellow color denotes the  
 278 fiber and the blue color denotes the matrix. For investigating the effect of the bias electric field on

(a)

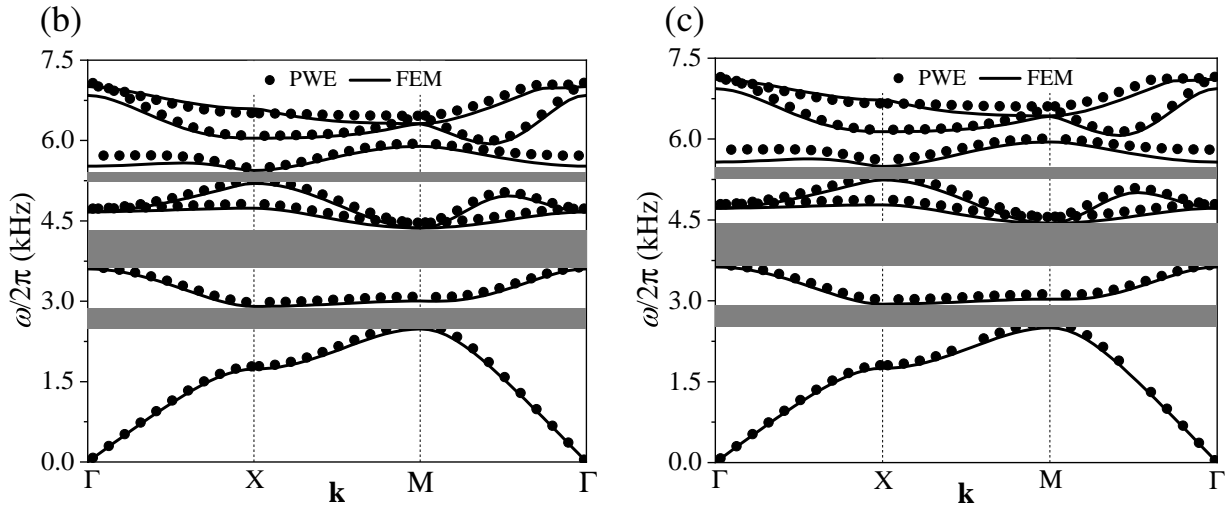
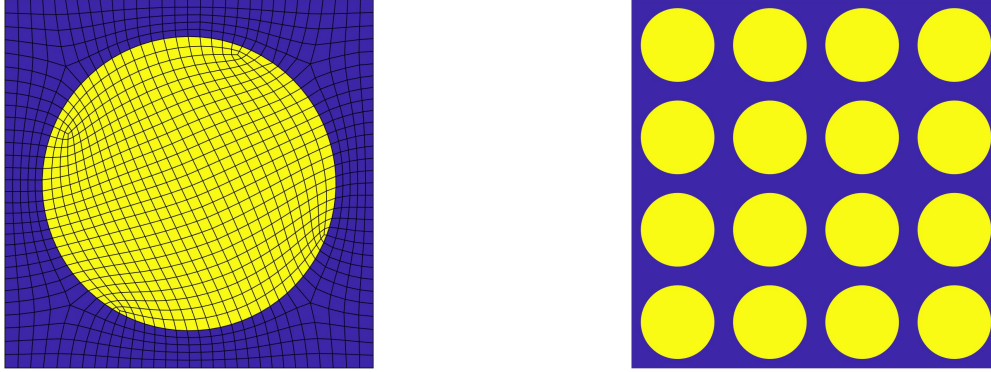


Figure 5: Influence of the bias electric field on the band structure of a DE composite with circular fiber and comparison of FEM results (solid lines) with the plane wave expansion method (PWE) results (symbols): (a) Unit cell (left) and periodic matrix (right), band diagrams (b) when bias electric field  $e_3 = 0$ , and (c) when bias electric field  $e_3 = 300$  MV/m.

279 the band diagram, we perform two cases, one without bias electric field ( $e_3 = 0$ ) and the other with  
 280 bias electric field  $e_3 = 300$  MV/m. For both cases, without and with bias electric field, Figs. 5b and  
 281 5c, respectively, compare the band structure computed using the finite element framework presented  
 282 in this work and the plane wave expansion method (PWE) (Shmuel, 2013). The plot shows a very  
 283 good agreement between FEM and PWE, validating our finite element framework. From the band  
 284 diagrams, it is evident that the width of the widest gap at  $e_3 = 0$ , i.e., ( $\Delta\omega/2\pi = 0.7626$  kHz), is  
 285 smaller than that at  $e_3 = 300$  MV/m, i.e., ( $\Delta\omega/2\pi = 0.8073$  kHz), denoting an increase in the band  
 286 gap width of 5.86%. This example suggests that the bias electric field has a favorable impact as it  
 287 improves the maximization of band gap widths.

## 288 6.2. Topology optimization results

289 In this section, first, we present the topologies for the maximization of the band gap width  
 290 between the first four adjacent bands (i.e., 1<sup>st</sup> and 2<sup>nd</sup> bands, 2<sup>nd</sup> and 3<sup>rd</sup> bands, 3<sup>rd</sup> and 4<sup>th</sup> bands,

Table 2: Optimized band gaps and fiber volume fractions, when maximizing gaps between two different adjacent bands.

Bias electric field ( $e_3$ ) $\rightarrow$	150 MV/m		300 MV/m	
	Band gap	Fiber fraction	Band gap	Fiber fraction
1 <sup>st</sup> and 2 <sup>nd</sup> bands	1.58	0.65	1.71	0.66
2 <sup>nd</sup> and 3 <sup>rd</sup> bands	1.94	0.58	2.25	0.57
3 <sup>rd</sup> and 4 <sup>th</sup> bands	1.73	0.57	2.08	0.58
4 <sup>th</sup> and 5 <sup>th</sup> bands	4.31	0.67	4.61	0.68

291 & 4<sup>th</sup> and 5<sup>th</sup> bands) and identify the two adjacent bands that have the largest optimized band gap  
 292 in the audible frequency range. For these four optimization cases, we consider two values of the  
 293 applied electric field, i.e.,  $e_3 = 150$  MV/m and  $e_3 = 300$  MV/m, and discretize the unit cell by  
 294  $20 \times 20$ , bi-linear quadrilateral elements. The initial material distribution of the unit cells is taken  
 295 to be random. The resulting designs of the unit cells that optimize the band gap widths between  
 296 the first four adjacent bands at applied electric field  $e_3 = 150$  MV/m and  $e_3 = 300$  MV/m are  
 297 depicted in the left panels of Figs. 6 and 7, respectively. In both figures, the middle panels represent  
 298 the periodic matrices composed of four optimized unit cells, while the right panels show the band  
 299 diagrams corresponding to the optimized unit cells depicted in the left panels. The estimates of  
 300 the optimized band gaps between the first four adjacent bands and the corresponding fiber volume  
 301 fractions for both the applied electric field values are listed in Table 2. From Table 2 and the left  
 302 panels of Figs. 6 and 7, we observe the maximum band gap width when the band gap is optimized  
 303 between the 4<sup>th</sup> and 5<sup>th</sup> bands. At  $e_3 = 150$  MV/m, the value of the maximal band gap width in  
 304 the audible frequency range is 4.31kHz and the corresponding fiber volume fraction is 0.67. The  
 305 maximal band gap width achieved in the audible frequency range at  $e_3 = 300$  MV/m, is 4.61kHz  
 306 with 0.68 fiber volume fraction.

307 Next, for the identified adjacent bands (i.e., 4<sup>th</sup> and 5<sup>th</sup> bands) representing maximum optimized  
 308 band gap in the audible frequency range, we present the optimized designs for different initial  
 309 layouts of the unit cells. We consider three initial layouts of the unit cells (fully random, single  
 310 central square fiber inclusion, and fiber inclusions at multiple locations) as shown in Table 3. For  
 311 these three initial layouts, the iteration history of the objective function and the evolution of the  
 312 optimal topology of the unit cells at applied electric fields  $e_3 = 150$  MV/m and  $e_3 = 300$  MV/m  
 313 are represented in Figs. 8 and 9, respectively. In both figures, the left columns show the iteration  
 314 history of the objective function and the evolution of the unit cell structure for a random initial  
 315 material distribution; the middle columns show the same data for an initial design consisting of  
 316 a central square fiber inclusion; and the right columns show the same data for an initial design  
 317 with fiber inclusions at multiple locations. From Figs. 8 and 9, we observe that the optimized  
 318 topologies depend on the initial layouts. This phenomenon of dependency on the initial layouts for  
 319 the unconstrained band gap maximization problem has been previously described in the literature  
 320 (Yi et al., 2019; Li et al., 2016b) and is somewhat expected in gradient-based optimization. From  
 321 the plots of the iteration histories of the objective function, we observe that the objective function  
 322 increases rapidly at the starting stage of the topology optimization process and then the convergence  
 323 rate becomes significantly slowed down over the iterations. The estimates of the optimized band  
 324 gaps and the corresponding fiber volume fractions for all three initial layouts and both the values of



Figure 6: Unit cells (left), periodic matrices composed of  $4 \times 4$  unit cells (middle), and band diagrams (right) of the optimized results when maximizing the band gap between (a) 1<sup>st</sup> and 2<sup>nd</sup> bands, (b) 2<sup>nd</sup> and 3<sup>rd</sup> bands, (c) 3<sup>rd</sup> and 4<sup>th</sup> bands, and (d) 4<sup>th</sup> and 5<sup>th</sup> bands, when bias electric field  $e_3 = 150$  MV/m.

325 the applied electric field are listed in Table 3. As evident from Table 3, the third initial guess (fiber  
 326 inclusions at multiple locations) for the unit cell layout is best among all the three initial guesses,

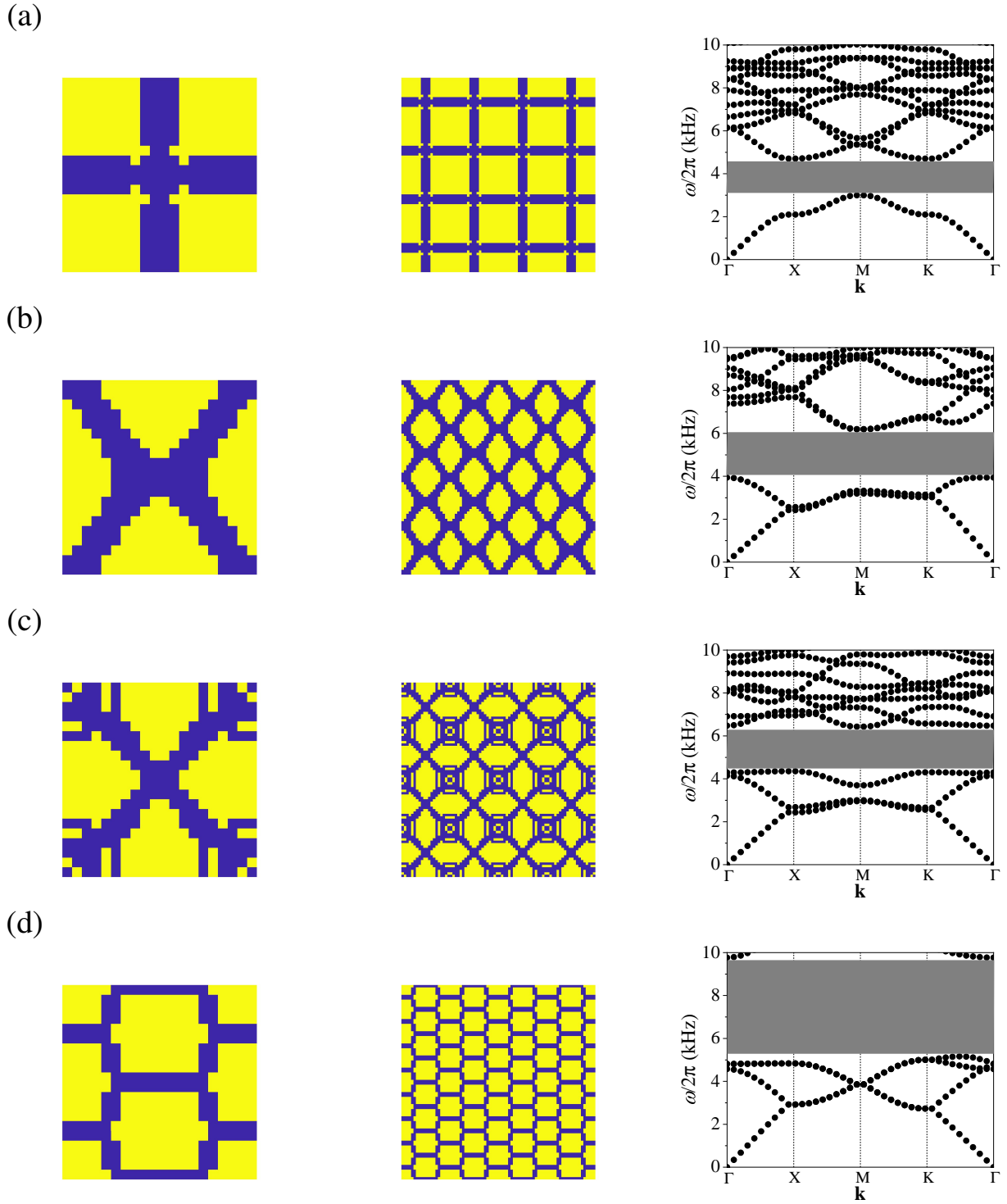


Figure 7: Unit cells (left), periodic matrices composed of  $4 \times 4$  unit cells (middle), and band diagrams (right) of the optimized results when maximizing the band gap between (a) 1<sup>st</sup> and 2<sup>nd</sup> bands, (b) 2<sup>nd</sup> and 3<sup>rd</sup> bands, (c) 3<sup>rd</sup> and 4<sup>th</sup> bands, and (d) 4<sup>th</sup> and 5<sup>th</sup> bands, when bias electric field  $e_3 = 300$  MV/m.

327 as it shows the maximum optimized band gap for both values of the applied electric fields. The  
 328 maximum band gap achieved at  $e_3 = 150$  MV/m is 4.37 kHz and that at  $e_3 = 300$  MV/m is

Table 3: Effect of initial material layout on the optimized band gaps and fiber volume fractions for maximization of band gap between 4<sup>th</sup> and 5<sup>th</sup> bands.

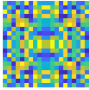


Initial material layout →						
Bias electric field ( $e_3$ )	Band gap	Fiber fraction	Band gap	Fiber fraction	Band gap	Fiber fraction
150 MV/m	4.31 kHz	0.67	4.30 kHz	0.68	4.37 kHz	0.68
300 MV/m	4.61 kHz	0.68	4.51 kHz	0.68	4.61 kHz	0.68

Table 4: Effect of mesh size on the optimized band gaps and fiber volume fractions for maximization of band gap between 4<sup>th</sup> and 5<sup>th</sup> bands.

Mesh density →	20×20		30×30		40×40	
Bias electric field ( $e_3$ )	Band gap	Fiber fraction	Band gap	Fiber fraction	Band gap	Fiber fraction
150 MV/m	4.37 kHz	0.680	4.33 kHz	0.715	4.30 kHz	0.680
300 MV/m	4.61 kHz	0.680	4.56 kHz	0.706	4.53 kHz	0.680

329 equal to 4.61 kHz. The fiber volume fractions corresponding to optimized layouts are the same for  
 330 both applied electric field and are equal to 0.68. As evident from the convergence history plots,  
 331 for the third initial layout of the unit cell, the topology optimization process converges faster in  
 332 comparison to the other two initial layouts. This is expected because it utilizes an educated initial  
 333 guess.

334 Next, we investigate the dependence of the optimized band gaps and the unit cell designs  
 335 on the FE mesh resolution, that affects the design resolution. For this purpose, we study the  
 336 maximization of band gap width between the 4<sup>th</sup> and 5<sup>th</sup> bands (i.e., having the highest band gaps in  
 337 the audible frequency range). For mesh dependency analyses, we discretize the unit cell by 20×20,  
 338 30×30, and 40×40 bi-linear square finite elements, and perform the topology optimizations for  
 339 maximizing the band gaps at the aforementioned two values of the applied electric field. For all  
 340 three mesh densities, we consider the same initial layout of the unit cell, i.e., the third layout of the  
 341 aforementioned discussion for which we obtained the maximum at both the applied electric fields.  
 342 The optimized designs of the unit cell and the corresponding band diagrams for 20×20, 30×30,  
 343 and 40×40 mesh densities and at  $e_3 = 150$  MV/m are compared in the left, middle and right panels  
 344 of Fig. 10a, respectively. For both values of bias electric field, the estimates of the optimized band  
 345 gaps and the corresponding fiber volume fractions at the aforementioned three mesh densities are  
 346 listed in Table 4. From the table, it is evident that the value of the optimized band gap decreases  
 347 with an increase in the mesh density for both the values of the bias electric field. This is attributed  
 348 to the effect of FE mesh refinement on the evaluation of the band gap. Interestingly, at 20×20 and  
 349 40×40 mesh density, we obtain the same designs of the unit cell and fiber volume fractions for both  
 350 values of the applied electric field.

351 Further, for a one-to-one comparison of the optimized unit cell structures obtained at different  
 352 mesh sizes, we evaluate the band gaps for all three optimized structures on a 120×120 mesh  
 353 resolution. This resolution is chosen such that all optimized designs can be projected precisely

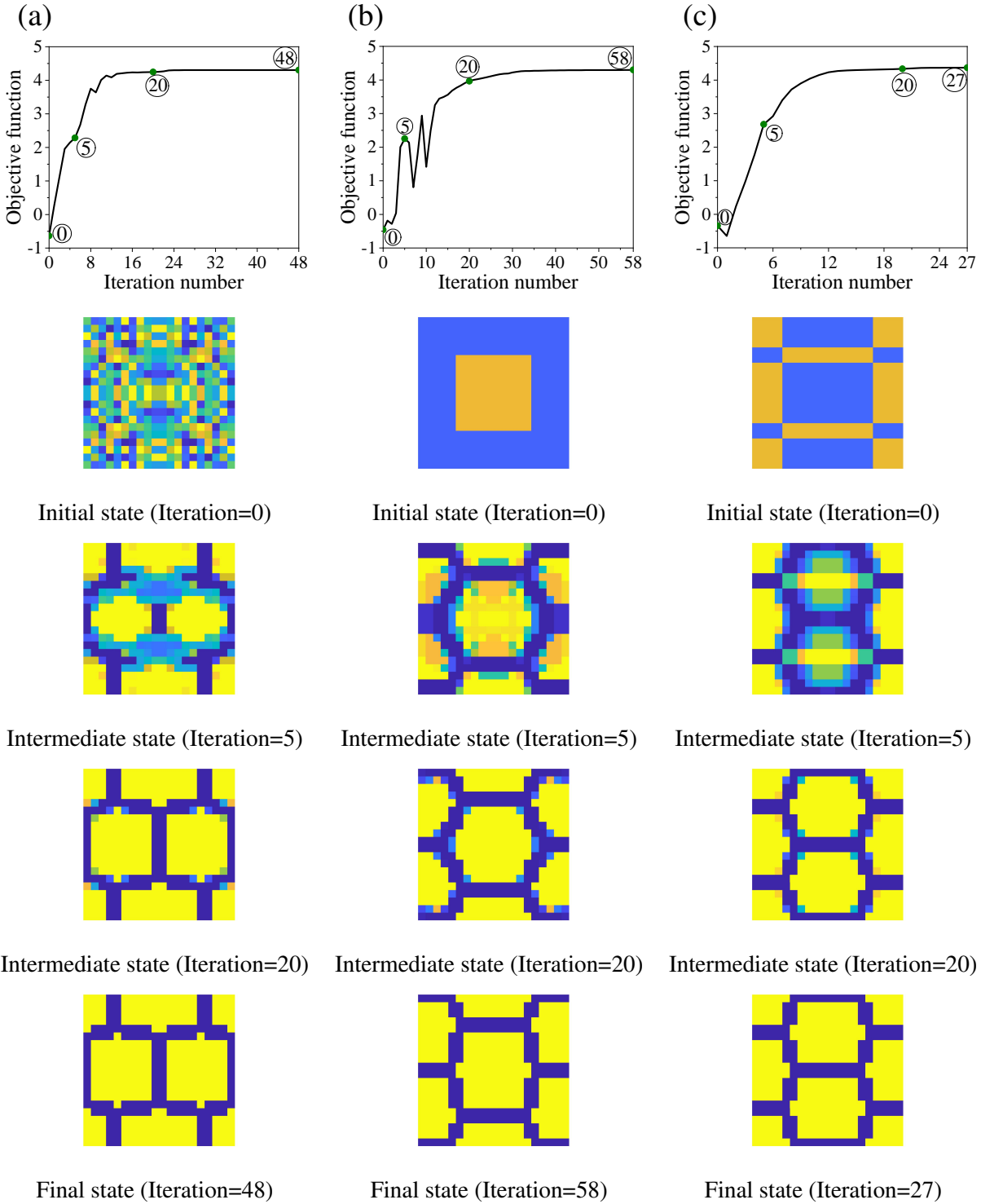


Figure 8: Optimization history and the layout evolution history of the unit cells for maximizing the band gap between 4<sup>th</sup> and 5<sup>th</sup> bands at bias electric field  $e_3 = 150$  MV/m, for various initial layouts of the unit cells: (a) fully random; (b) central square fiber inclusion; and (c) fiber inclusions at multiple locations.

354 to a common mesh. Table 5 enlists the band gap values evaluated on a  $120 \times 120$  mesh resolution  
 355 for the optimized unit cells obtained at the aforementioned three mesh densities and two values

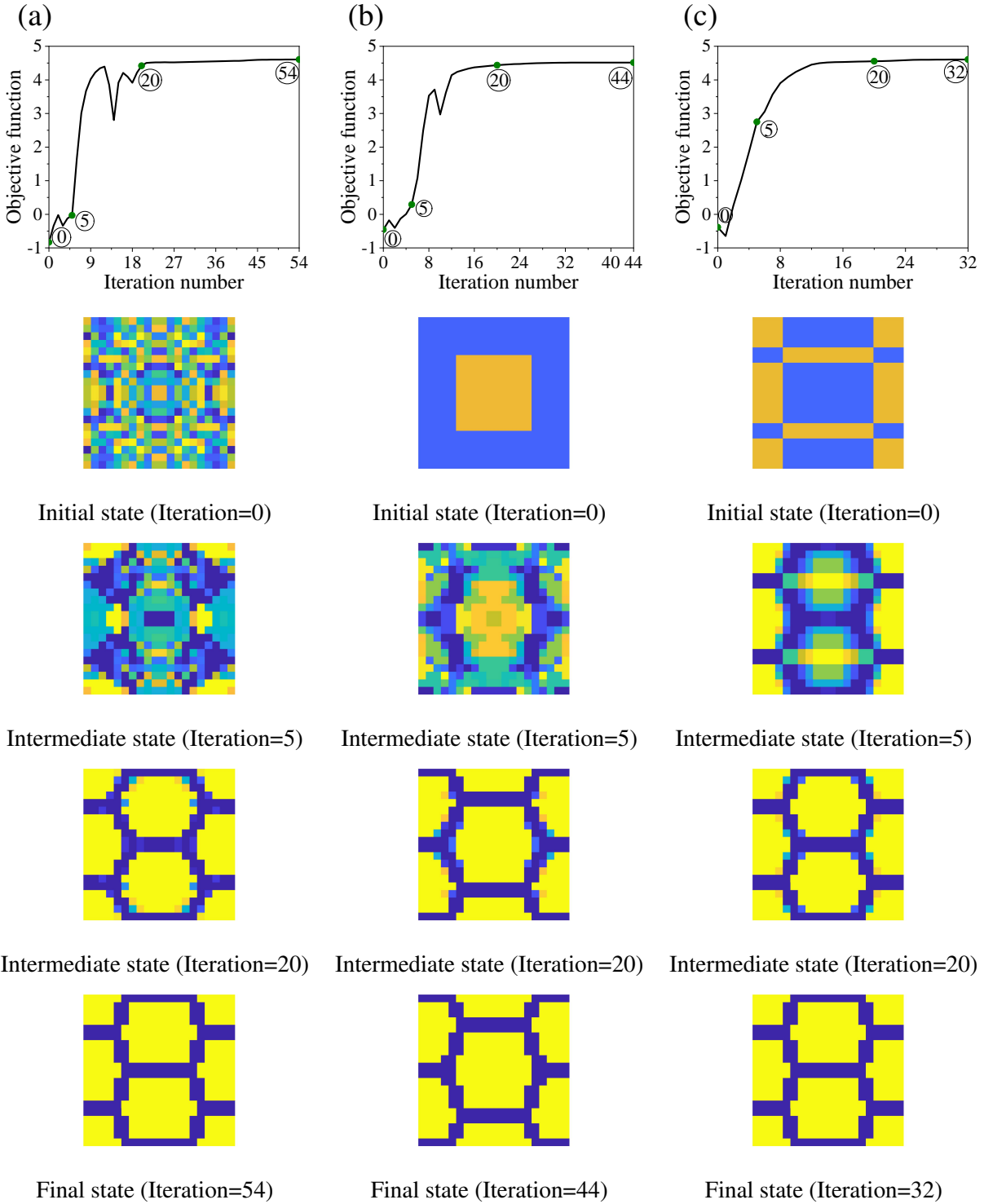


Figure 9: Optimization history and the layout evolution history of the unit cells for maximizing the band gap between 4<sup>th</sup> and 5<sup>th</sup> bands at bias electric field  $e_3 = 300$  MV/m, for various initial layouts of the unit cells: (a) fully random; (b) central square fiber inclusion; and (c) fiber inclusions at multiple locations.

356 of bias electric field. The band diagrams evaluated at  $120 \times 120$  mesh resolution of the unit cells  
 357 optimized at three mesh sizes are shown in Fig. 11. From Table 5, we can see that as the design

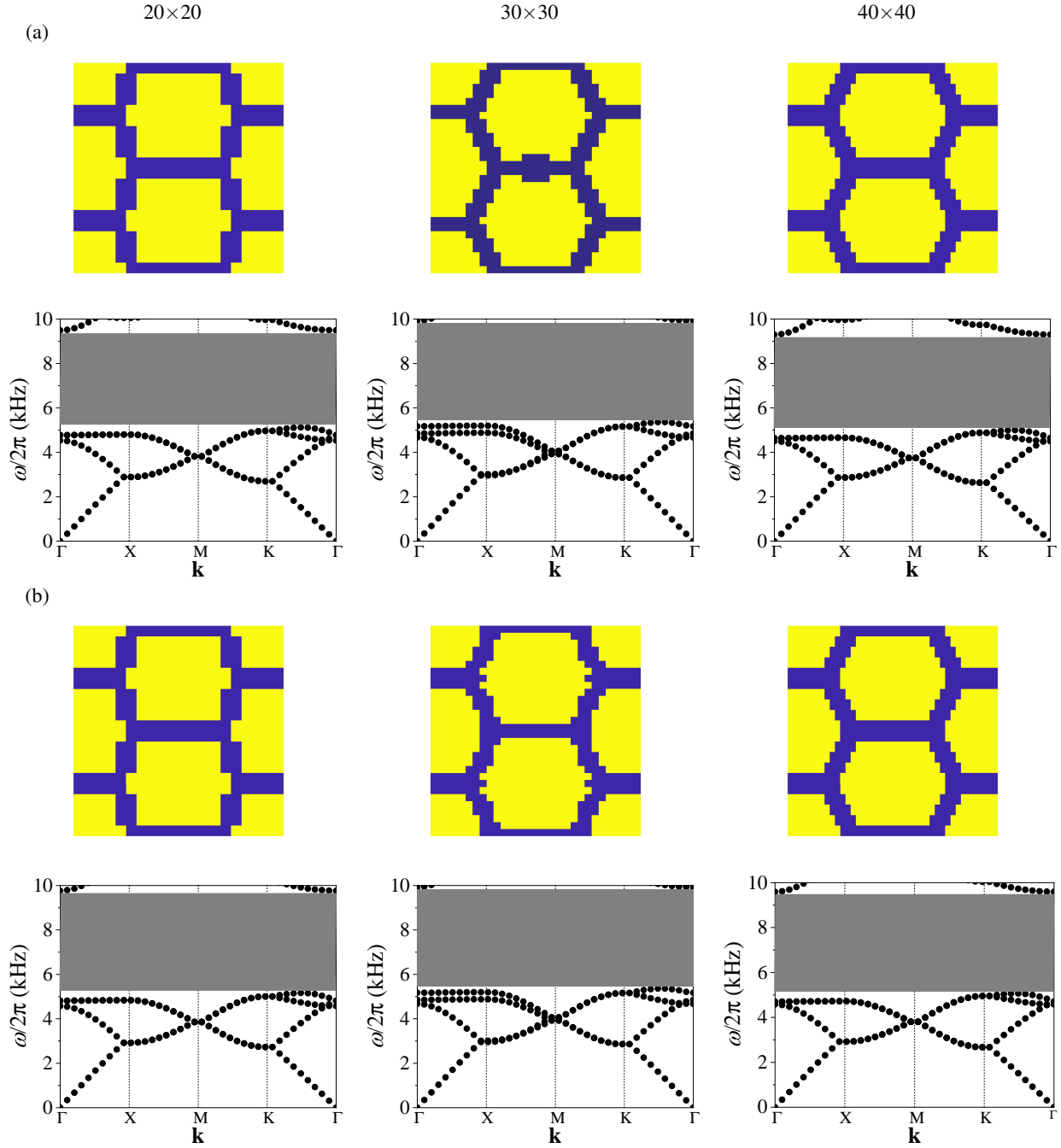


Figure 10: Effect of mesh size (left,  $20 \times 20$ ; middle,  $30 \times 30$ ; right,  $40 \times 40$ ) on the optimized layouts of the unit cells for maximizing the band gap between 4<sup>th</sup> and 5<sup>th</sup> bands, when bias electric field (a)  $e_3 = 150$  MV/m, and (b)  $e_3 = 300$  MV/m.

358 resolution increases, so does the width of the optimized band gap. This demonstrates the efficacy  
 359 of the topology optimization method: better performance can be achieved by increasing the design  
 360 resolution, hence expanding the design space. The unit cell layouts obtained from the optimization  
 361 at  $40 \times 40$  mesh density show the maximum band gap for both bias electric fields. For  $120 \times 120$   
 362 mesh resolution, the value of maximum band gap achieved at  $e_3 = 150$  MV/m is 4.24 kHz with

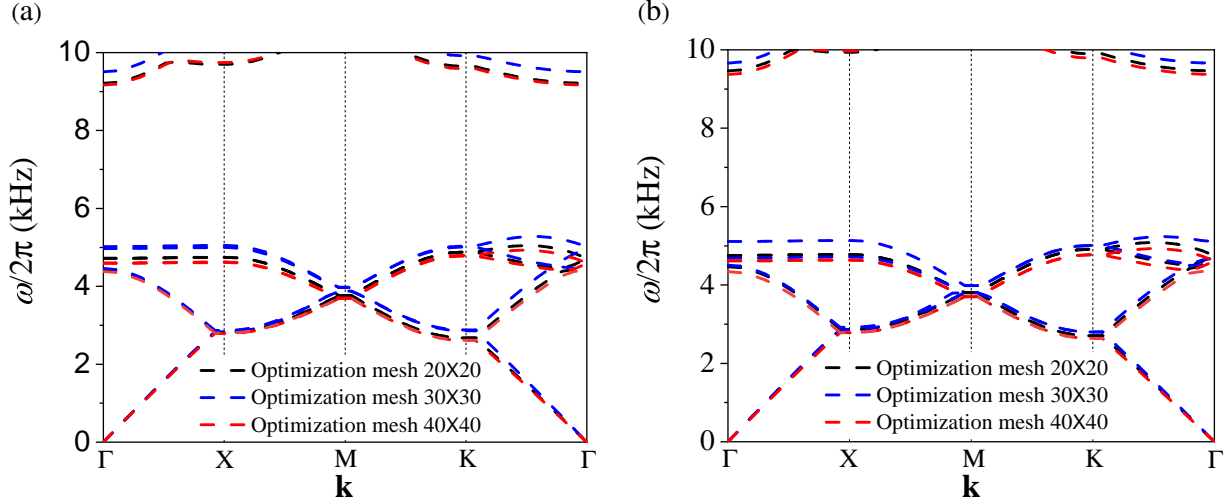


Figure 11: Comparison of the band diagrams for  $120 \times 120$  mesh resolution of the unit cells optimized at  $20 \times 20$ ,  $30 \times 30$ , and  $40 \times 40$  mesh densities, (a) when bias electric field  $e_3 = 150$ , and (b) when bias electric field  $e_3 = 300$  MV/m.

363 0.68 fiber volume fraction and that at  $e_3 = 300$  MV/m is equal to 4.44 kHz with the same fiber  
 364 volume fraction of 0.68.

Table 5: Band gap between 4<sup>th</sup> and 5<sup>th</sup> bands at  $120 \times 120$  mesh resolution for the unit cells optimized on  $20 \times 20$ ,  $30 \times 30$  and  $40 \times 40$  mesh densities.

Optimization mesh density $\rightarrow$	20 $\times$ 20		30 $\times$ 30		40 $\times$ 40	
Bias electric field ( $e_3$ ) $\rightarrow$	150 MV/m	300 MV/m	150 MV/m	300 MV/m	150 MV/m	300 MV/m
Optimized unit cells						
Band gap at $120 \times 120$ mesh resolution	4.17 kHz	4.38 kHz	4.22 kHz	4.43 kHz	4.24 kHz	4.44 kHz

365 Finally, we discuss the advantages of the gradient-based topology optimization framework  
 366 developed in this paper over the method based on PWE and a genetic algorithm (GA) for maximization  
 367 of band gaps in dielectric elastomers (Bortot et al., 2018). For this purpose, we compare the  
 368 optimized designs of the unit cells and the corresponding optimized band gaps obtained using  
 369 both methods of optimization. For one-to-one comparison, we consider the design structures  
 370 optimized at the same mesh density i.e.,  $20 \times 20$ . Figures 12a and 12b show the designs of the  
 371 optimized unit cell obtained using gradient-based and GA-based topology optimization methods,  
 372 respectively, at bias electric field  $e_3 = 150$ . The fiber volume fraction for the unit cell optimized  
 373 using a gradient-based optimization scheme is 0.68 and while for that optimized using GA is equal  
 374 to 0.64. The band diagrams for optimized unit cells in Figs. 12a and 12b are shown in Fig. 12c.  
 375 From the band diagrams, we observe the larger band gap for the unit cell optimized using the  
 376 gradient-based formulation (4.37 kHz) in comparison to the one optimized using GA (4.13 kHz).  
 377 The present approach also holds a significant computational advantage: the computational cost of

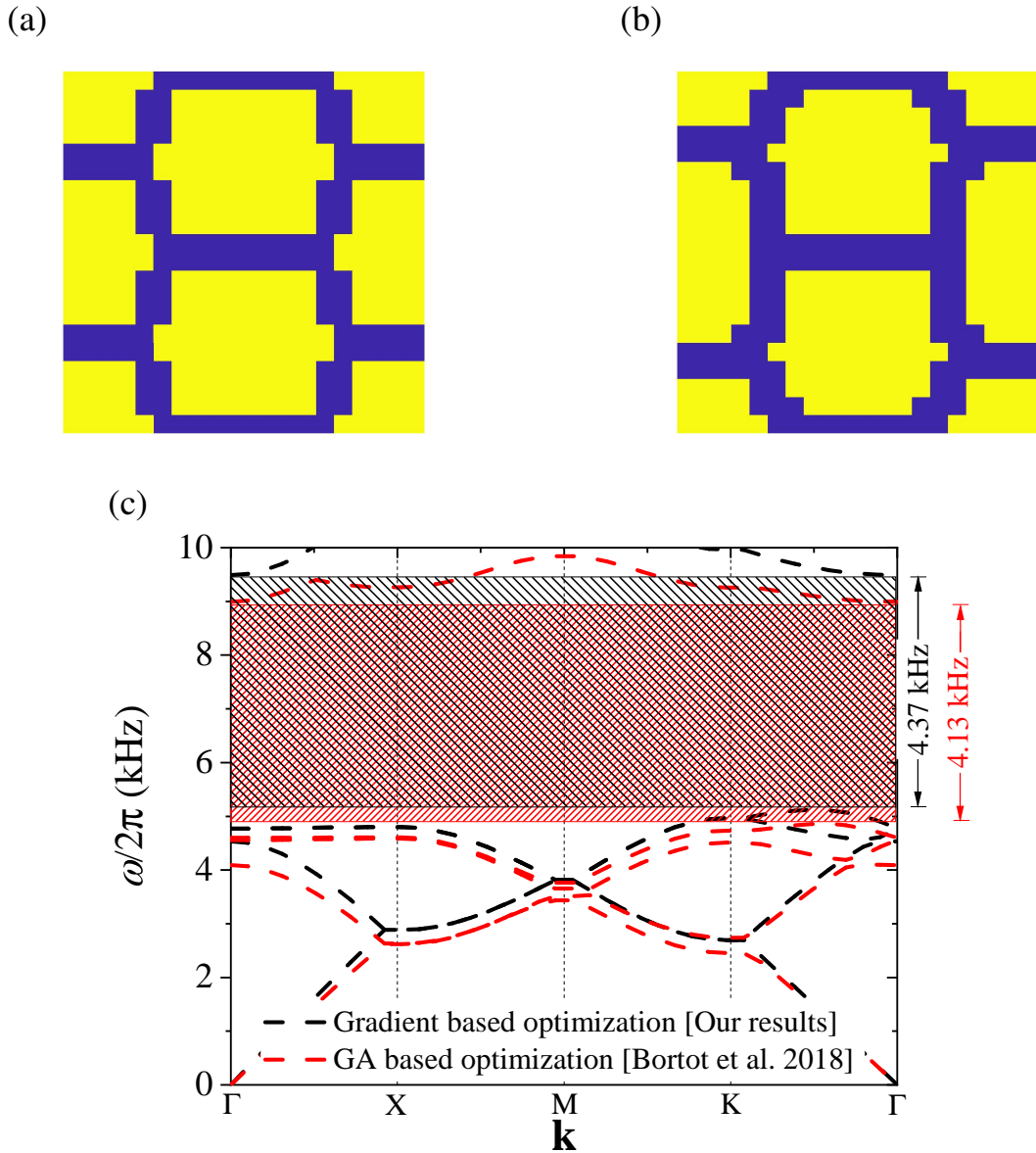


Figure 12: Designs of the unit cells optimized using (a) the gradient based optimization formulation presented in this paper and (b) a GA-based optimization method (Bortot et al., 2018). (c) Comparison of the corresponding band diagrams.

378 the GA is higher by several orders of magnitude, and this limits the achievable design resolution.  
 379 For example, Bortot et al. (2018) reported that 12,500 function evaluations were required for GA  
 380 to converge in a problem with 100 design variables. Herein, these problems are solved in less  
 381 than 60 design cycles, where each cycle requires a single function evaluation and the computation  
 382 of gradients. The cost of computing gradients can be estimated as roughly the same as a single  
 383 function evaluation. As shown above, larger design freedom can yield better band gap performance,  
 384 and this can only be achieved with the gradient-based approach that easily scales to finer mesh  
 385 resolutions.

## 386 7. Summary

387 When subjected to electric fields, dielectric elastomers undergo finite deformations and their  
388 instantaneous moduli change. These features can be exploited to electrostatically tune the width of  
389 band gaps, across which waves cannot propagate in dielectric elastomer composites.

390 The width of these gaps in the actuated state is a function of the microstructure of the composite.  
391 To date, to identify optimal microstructures with wider gaps in the actuated state, topology optimization  
392 methods based on metaheuristics, specifically genetic algorithms, were used. These methods,  
393 which utilize only function evaluations without any gradient information, are limited by the computational  
394 cost that increases exponentially with the number of design variables.

395 In this work, we have developed a gradient-based topology optimization method, which utilizes  
396 information from the gradient of the objective function in order to iteratively update the design  
397 variables (Svanberg, 1987). The case study to which we have developed the method is of incremental  
398 anti-plane shear waves, propagating in a planar dielectric elastomer composite that is subjected to  
399 axial electric fields (Shmuel, 2013; Getz & Shmuel, 2017; Bortot & Shmuel, 2017). Specifically,  
400 we have developed a finite element formulation to solve the incremental dynamical problem, and  
401 extract the band diagram of the composite. Based on this formulation, we have derived an implemented  
402 a fully analytical sensitivity analysis for computing the gradient of the objective function: the width  
403 of the gap in the audible range, at two prescribed electric fields.

404 In comparison with the genetic algorithm-based method (Bortot et al., 2018), our gradient-based  
405 method not only identified microstructures with wider gaps: it also reached these microstructures  
406 in an orders-of-magnitude cheaper computational cost. Thus, the gradient-based approach easily  
407 scales to finer mesh resolutions.

## 408 Acknowledgement

409 This research was supported by the Israel Science Foundation, funded by the Israel Academy of  
410 Sciences and Humanities (Grant no. 2061/20), the United States-Israel Binational Science Foundation  
411 (Grant no. 2014358), and Ministry of Science and Technology (grant no. 880011).

## 412 Appendix: Smooth formulation with approximate maximum and minimum eigenfrequencies 413 along the wave vector $\mathbf{k}$

414 The objective function of the optimization problem in Eq. (36) is not strictly differentiable,  
415 because the  $\mathbf{k}$ -vector(s) corresponding to the maximum and minimum eigenfrequencies may change  
416 during the optimization iterations. Here, we present a topology optimization formulation in which  
417 the maximum and minimum values of eigenfrequencies along the wave vector  $\mathbf{k}$  are approximated  
418 using a  $p$ -norm function, and compare the results for one test case to those in Section 5. We examine  
419 the maximization of the band gap between the fourth and fifth bands which have a maximum  
420 optimized band gap in the audible frequency range.

421 Utilizing the standard  $p$ -norm measure (Duysinx & Sigmund, 1998; Le et al., 2010), the maximum  
422 and minimum values of the eigenfrequencies corresponding to lower and upper bands, respectively,

423 are approximated as

$$\omega_{\max}^{PN} = \left( \sum_{i=1}^n (\omega_i)^p \right)^{\frac{1}{p}} ; \quad \omega_{\min}^{PN} = \frac{1}{\left( \sum_{i=1}^n \left( \frac{1}{\omega_i} \right)^p \right)^{\frac{1}{p}}}, \quad (\text{A.1})$$

424 where,  $p$  is the  $p$ -norm parameter,  $\omega_i$  represents the value of the eigenfrequency corresponding to  
 425 the  $i^{\text{th}}$  point along the wave vector  $\mathbf{k}$ . In this work, we took  $p = 80$  and  $n = 40$  points along the  
 426 wave vector  $\mathbf{k}$ .

427 The modified version of the objective function is written as

$$f^{PN} = \begin{cases} 10 \text{ kHz} - \omega_{\max}^{PN}/2\pi & \text{if } \min \omega_{j+1}(\xi, \mathbf{k})/2\pi \geq 10\text{kHz}, \\ (\omega_{\min}^{PN} - \omega_{\max}^{PN})/2\pi & \text{if } \min \omega_{j+1}(\xi, \mathbf{k})/2\pi \leq 10\text{kHz}. \end{cases} \quad (\text{A.2})$$

428 and the sensitivities of the maximum and minimum frequencies approximated using  $p$ -norm with  
 429 respect to design variable  $\xi_e$  are expressed as

$$\begin{aligned} \frac{\partial \omega_{\max}^{PN}}{\partial \xi_e} &= \left( \sum_{i=1}^n (\omega_i)^p \right)^{\frac{1}{p}-1} \left( \sum_{i=1}^n (\omega_i)^{p-1} \frac{\partial \omega_i}{\partial \xi_e} \right); \\ \frac{\partial \omega_{\min}^{PN}}{\partial \xi_e} &= \left( \sum_{i=1}^n \left( \frac{1}{\omega_i} \right)^p \right)^{-1-\frac{1}{p}} \left( \sum_{i=1}^n \left( \frac{1}{\omega_i} \right)^{p+1} \frac{\partial \omega_i}{\partial \xi_e} \right), \end{aligned} \quad (\text{A.3})$$

430 in which the derivative  $\frac{\partial \omega_i}{\partial \xi_e}$  is evaluated using Eq. (39). Further, utilizing Eq. (A.3), we evaluated

431 the gradient of the modified version of the objective function  $\frac{\partial f^{PN}}{\partial \xi_e}$  used for updating the design  
 432 variables.

433 The optimized layouts of the unit cell, the corresponding band diagrams, and objective function  
 434 history obtained using the aforementioned  $p$ -norm formulation, for the maximization of the band  
 435 gap between the 4<sup>th</sup> and 5<sup>th</sup> bands are shown in Figs. 13a and 13b, when bias electric field is equal  
 436 to  $e_3 = 150$  MV/m and  $e_3 = 300$  MV/m, respectively. From the optimized unit cell designs, we  
 437 observe that the designs are the same as those obtained using the original formulation (Figs. 8c and  
 438 9c) for both values of bias electric field. In Fig. 14, we show that the location of  $\omega_{\max}$  and  $\omega_{\min}$  along  
 439 the wave vector  $\mathbf{k}$  is almost constant same for all iterations of the non-smooth formulation. This  
 440 explains why the same designs are obtained using both formulations. However, from the right panel  
 441 of Figs. 13a and 13b, we observe that the optimization with  $p$ -norms takes 41 (for  $e_3 = 150$  MV/m)  
 442 and 77 (for  $e_3 = 300$  MV/m) iterations to converge, which consumes 14 (for  $e_3 = 150$  MV/m) and  
 443 39 (for  $e_3 = 300$  MV/m) more iterations in comparison to the non-smooth formulation (Figs. 8c and  
 444 9c). Further, the computational cost of optimization with the  $p$ -norm formulation is significantly  
 445 higher in comparison to the non-smooth formulation, due to the evaluation of design sensitivities  
 446 or the derivatives of eigenvalues corresponding to different values of wave-vector  $\mathbf{k}$  along the first  
 447 Brillouin zone.

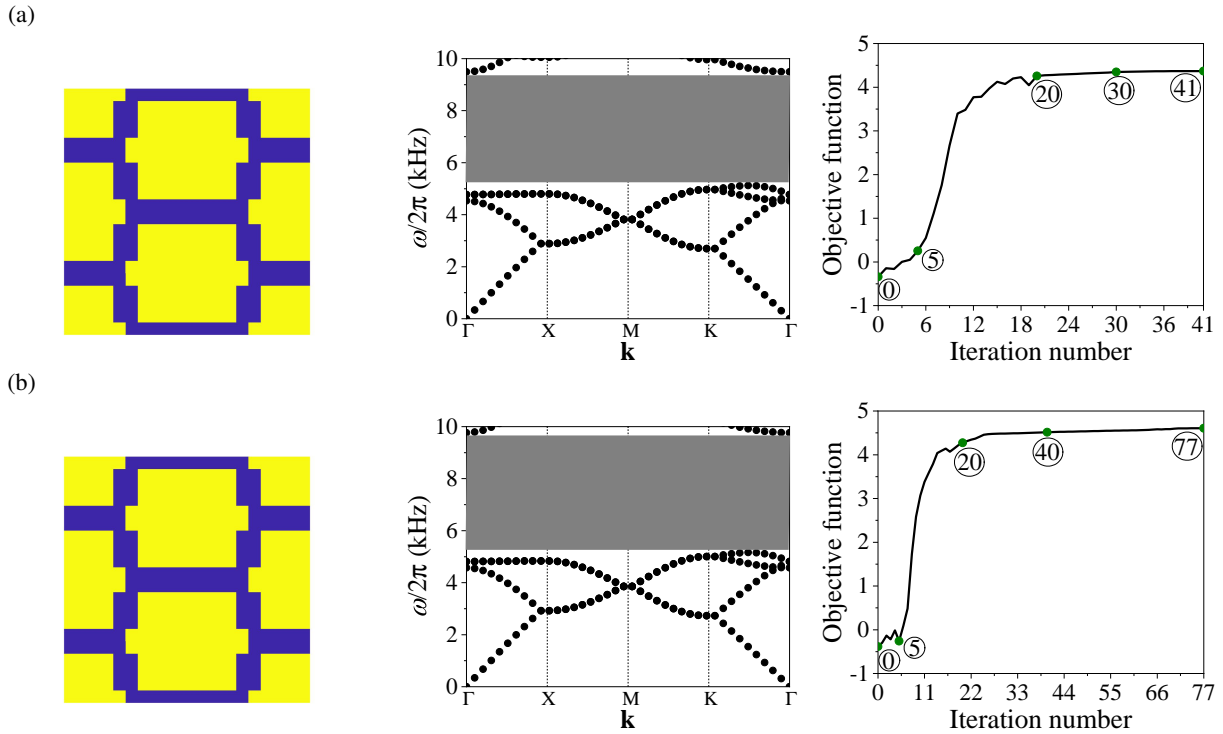


Figure 13: Unit cells (left), band diagrams (middle), and objective function history (right) when maximizing the band gap between 4<sup>th</sup> and 5<sup>th</sup> bands using the  $p$ -norm formulation, (a) when bias electric field  $e_3 = 150$  MV/m, and (b) when bias electric field  $e_3 = 300$  MV/m,

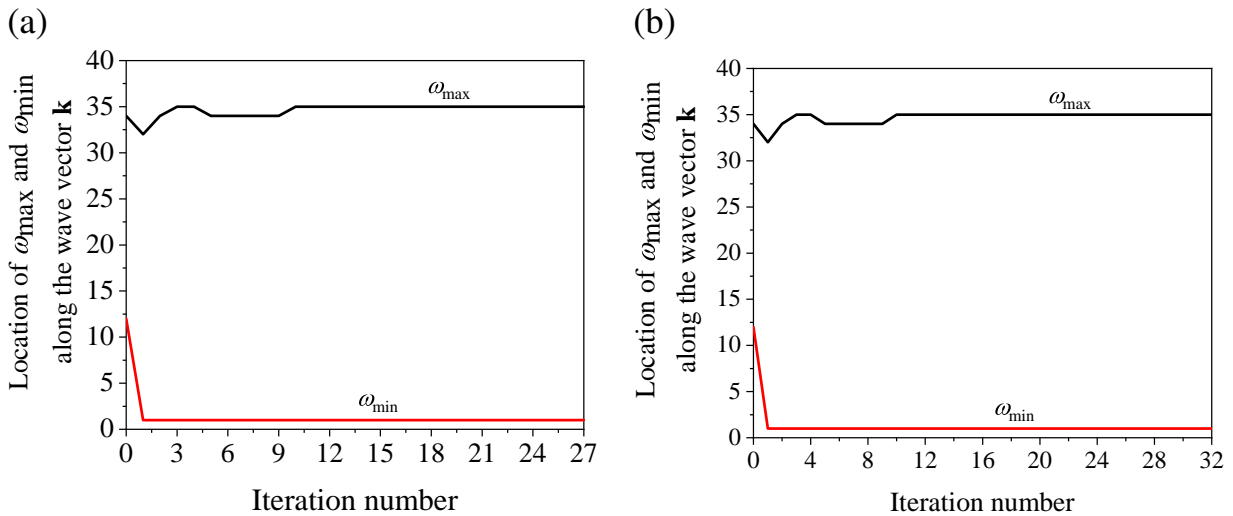


Figure 14: Variation of the location of the  $\omega_{\max}$  and  $\omega_{\min}$  along the wave vector  $\mathbf{k}$ , for the optimization of the band gap between 4<sup>th</sup> and 5<sup>th</sup> bands using discrete formulation (Section 5), at (a) bias electric field  $e_3 = 150$  MV/m and (c) bias electric field  $e_3 = 300$  MV/m.

448 **References**

449 Bendsøe, M., & Kikuchi, N. (1988). Generating optimal topologies in structural design using  
 450 a homogenization method. *Computer Methods in Applied Mechanics and Engineering*,

451 71, 197 – 224. URL: [http://www.sciencedirect.com/science/article/pii/](http://www.sciencedirect.com/science/article/pii/0045782588900862)  
452 0045782588900862. doi:[https://doi.org/10.1016/0045-7825\(88\)90086-2](https://doi.org/10.1016/0045-7825(88)90086-2).

453 Bilal, O., & Hussein, M. (2011). Ultrawide phononic band gap for combined in-plane and out-of-  
454 plane waves. *Physical Review E*, 84, 065701. doi:10.1103/PhysRevE.84.065701.

455 Bortot, E., Amir, O., & Shmuel, G. (2018). Topology optimization of dielectric elastomers for wide  
456 tunable band gaps. *International Journal of Solids and Structures*, 143, 262–73.

457 Bortot, E., & Shmuel, G. (2017). Tuning sound with soft dielectrics. *Smart Materials and*  
458 *Structures*, 26, 045028.

459 De Pascalis, R., Donato, T., Ficarella, A., & Parnell, W. J. (2020). Optimal design of  
460 phononic media through genetic algorithm-informed pre-stress for the control of antiplane wave  
461 propagation. *Extreme Mechanics Letters*, 40, 100896.

462 Deaton, J. D., & Grandhi, R. V. (2014). A survey of structural and multidisciplinary continuum  
463 topology optimization: post 2000. *Structural and Multidisciplinary Optimization*, 49, 1–38.

464 DeBotton, G., Tevet-Deree, L., & Socolsky, E. A. (2007). Electroactive heterogeneous polymers:  
465 analysis and applications to laminated composites. *Mech. Adv. Mater. Struct.*, 14, 13–22.

466 Dorfmann, A., & Ogden, R. (2005). Nonlinear electroelasticity. *Acta Mechanica*, 174, 167–83.

467 Dorfmann, A., & Ogden, R. W. (2010). Electroelastic waves in a finitely deformed electroactive  
468 material. *IMA Journal of Applied Mathematics*, 75, 603–36.

469 Duysinx, P., & Sigmund, O. (1998). New developments in handling stress constraints in optimal  
470 material distribution. In *7th AIAA/USAF/NASA/ISSMO symposium on multidisciplinary analysis*  
471 *and optimization* (p. 4906).

472 Felippa, C. (2001). Introduction to finite element methods. multifreedom constraints ii (lecture  
473 notes).

474 Gazonas, G., Weile, D., Wildman, R., & Mohan, A. (2006). Genetic algorithm optimization of  
475 phononic bandgap structures. *International Journal of Solids and Structures*, 43, 5851–66.  
476 doi:10.1016/j.ijsolstr.2005.12.002.

477 Gei, M., Roccabianca, S., & Bacca, M. (2011). Controlling bandgap in electroactive polymer-based  
478 structures. *IEEE-ASME Trans. Mechatronics*, 16, 102–7.

479 Gei, M., Springhetti, R., & Bortot, E. (2013). Performance of soft dielectric laminated  
480 composites. *Smart Materials and Structures*, 22, 104014. URL: [https://doi.org/10.](https://doi.org/10.1088/0964-1726/22/10/104014)  
481 1088/0964-1726/22/10/104014. doi:10.1088/0964-1726/22/10/104014.

482 Getz, R., Kochmann, D. M., & Shmuel, G. (2017). Voltage-controlled complete stopbands in  
483 two-dimensional soft dielectrics. *International Journal of Solids and Structures*, 113, 24–36.

484 Getz, R., & Shmuel, G. (2017). Band gap tunability in deformable dielectric composite plates.  
485 *International Journal of Solids and Structures*, 128, 11–22.

- 486 Gu, G., Zou, J., Zhao, R., Zhao, X., & Zhu, X. (2018). Soft wall-climbing robots. *Science Robotics*,  
487 3.
- 488 Hajiesmaili, E., & Clarke, D. R. (2021). Dielectric elastomer actuators. *Journal of Applied Physics*,  
489 129, 151102.
- 490 Halkjær, O., Sigmund, & Jensen, J. (2006). Maximizing band gaps in plate structures.  
491 *Structural and Multidisciplinary Optimization*, 32, 263–75. doi:[https://doi.org/10.](https://doi.org/10.1007/s00158-006-0037-7)  
492 1007/s00158-006-0037-7.
- 493 Hedayatrasa, S., Abhary, K., Uddin, M., & Guest, J. (2016). Optimal design of tunable  
494 phononic bandgap plates under equibiaxial stretch. *Smart Materials and Structures*, 25, 055025.  
495 doi:<http://dx.doi.org/10.1088/0964-1726/25/5/055025>.
- 496 Hussein, M., Hamza, K., Hulbert, G., & Saitou, K. (2007). Optimal synthesis of 2d phononic  
497 crystals for broadband frequency isolation. *Waves in Random and Complex Media*, 17, 491–510.  
498 doi:10.1080/17455030701501869.
- 499 Jandron, M., & Henann, D. L. (2018). A numerical simulation capability for electroelastic wave  
500 propagation in dielectric elastomer composites: Application to tunable soft phononic crystals.  
501 *International Journal of Solids and Structures*, 150, 1–21.
- 502 Kim, C.-C., Lee, H.-H., Oh, K. H., & Sun, J.-Y. (2016). Highly stretchable, transparent ionic touch  
503 panel. *Science*, 353, 682–7.
- 504 Kittel, C., McEuen, P., & McEuen, P. (1996). *Introduction to solid state physics* volume 8. Wiley  
505 New York.
- 506 Kushwaha, M. S., Halevi, P., Dobrzynski, L., & Djafari-Rouhani, B. (1993). Acoustic band  
507 structure of periodic elastic composites. *Physical review letters*, 71, 2022.
- 508 Kushwaha, M. S., Halevi, P., Martinez, G., Dobrzynski, L., & Djafari-Rouhani, B. (1994). Theory  
509 of acoustic band structure of periodic elastic composites. *Physical Review B*, 49, 2313.
- 510 Le, C., Norato, J., Bruns, T., Ha, C., & Tortorelli, D. (2010). Stress-based topology optimization  
511 for continua. *Structural and Multidisciplinary Optimization*, 41, 605–20.
- 512 Li, W., Meng, F., Chen, Y., Li, Y. f., & Huang, X. (2019). Topology optimization of photonic and  
513 phononic crystals and metamaterials: a review. *Advanced Theory and Simulations*, 2, 1900017.
- 514 Li, Y., Huang, X., Meng, F., & Zhou, S. (2016a). Evolutionary topological design for phononic  
515 band gap crystals. *Structural and Multidisciplinary Optimization*, 54, 595–617. doi:10.1007/  
516 s00158-016-1424-3.
- 517 Li, Y. f., Huang, X., Meng, F., & Zhou, S. (2016b). Evolutionary topological design for phononic  
518 band gap crystals. *Structural and Multidisciplinary Optimization*, 54, 595–617.
- 519 Liu, W., Yoon, G. H., Yi, B., Choi, H., & Yang, Y. (2020). Controlling wave propagation in one-  
520 dimensional structures through topology optimization. *Computers & Structures*, 241, 106368.

- 521 Liu, Z., Wu, B., & He, C. (2014). Band-gap optimization of two-dimensional phononic crystals  
522 based on genetic algorithm and FPWE. *Waves in Random and Complex Media*, 24, 286–305.  
523 doi:10.1080/17455030.2014.901582.
- 524 Liu, Z., Wu, B., & He, C. (2016). Systematic topology optimization of solid-solid phononic crystals  
525 for multiple separate band-gaps with different polarizations. *Ultrasonics*, 65, 249–57. doi:10.  
526 1016/j.ultras.2015.09.017.
- 527 Lu, T., Shi, Z., Shi, Q., & Wang, T. (2016). Bioinspired bicipital muscle with fiber-constrained  
528 dielectric elastomer actuator. *Extreme Mechanics Letters*, 6, 75–81.
- 529 Lu, Y., Yang, Y., Guest, J., & Srivastava, A. (2017). 3-D phononic crystals with ultra-wide  
530 band gaps. *Scientific Reports*, 7, 43407 EP -. URL: [http://dx.doi.org/10.1038/  
531 srep43407](http://dx.doi.org/10.1038/srep43407).
- 532 Lustig, B., & Shmuel, G. (2018). On the band gap universality of multiphase  
533 laminates and its applications. *Journal of the Mechanics and Physics of Solids*,  
534 117, 37–53. URL: [http://www.sciencedirect.com/science/article/pii/  
535 S0022509618302321](http://www.sciencedirect.com/science/article/pii/S0022509618302321). doi:<https://doi.org/10.1016/j.jmps.2018.04.008>.
- 536 Meng, F., Li, Y., Li, S., Lin, H., Jia, B., & Huang, X. (2017). Achieving large band gaps in 2d  
537 symmetric and asymmetric photonic crystals. *Journal of Lightwave Technology*, 35, 1670–6.
- 538 Mohajer, M., Zhou, J., & Jiang, L. (2021). Small amplitude rayleigh-lamb wave propagation  
539 in a finitely deformed viscoelastic dielectric elastomer (de) layer. *International Journal  
540 of Solids and Structures*, 208-209, 93–106. URL: [https://www.sciencedirect.  
541 com/science/article/pii/S0020768320303917](https://www.sciencedirect.com/science/article/pii/S0020768320303917). doi:[https://doi.org/10.  
542 1016/j.ijsolstr.2020.10.006](https://doi.org/10.1016/j.ijsolstr.2020.10.006).
- 543 Oliveira, J., Pinho-da Cruz, J., Andrade-Campos, A., & Teixeira-Dias, F. (2010). Stress-and strain-  
544 based multifreedom constraints for periodic media optimisation. *Actas da EngOpt*, .
- 545 Ortigosa, R., & Martínez-Frutos, J. (2021). Multi-resolution methods for the topology optimization  
546 of nonlinear electro-active polymers at large strains. *Computational Mechanics*, (pp. 1–23).
- 547 Ortigosa, R., Martínez-Frutos, J., Ruiz, D., Donoso, A., & Bellido, J. (2021). Density-based  
548 topology optimisation considering nonlinear electromechanics. *Structural and Multidisciplinary  
549 Optimization*, (pp. 1–24).
- 550 Pelrine, R., Kornbluh, R., Pei, Q., & Joseph, J. (2000). High-speed electrically actuated elastomers  
551 with strain greater than 100%. *Science*, 287, 836–9.
- 552 Qian, X., & Sigmund, O. (2011). Isogeometric shape optimization of photonic crystals via coons  
553 patches. *Computer Methods in Applied Mechanics and Engineering*, 200, 2237–55.
- 554 Quinteros, L., Meruane, V., & Cardoso, E. L. (2021). Phononic band gap optimization in truss-  
555 like cellular structures using smooth p-norm approximations. *Structural and Multidisciplinary  
556 Optimization*, (pp. 1–12).

- 557 Sharma, A. K. (2020). Design of a command-shaping scheme for mitigating residual vibrations in  
558 dielectric elastomer actuators. *Journal of Applied Mechanics*, 87.
- 559 Sharma, A. K., Arora, N., & Joglekar, M. (2018). Dc dynamic pull-in instability of a  
560 dielectric elastomer balloon: an energy-based approach. *Proceedings of the Royal Society A:  
561 Mathematical, Physical and Engineering Sciences*, 474, 20170900.
- 562 Sharma, A. K., Kumar, P., Singh, A., Joglekar, D., & Joglekar, M. (2019). Electromechanical  
563 instability of dielectric elastomer actuators with active and inactive electric regions. *Journal of  
564 Applied Mechanics*, 86.
- 565 Sharma, A. K., Sheshkar, N., & Gupta, A. (2021). Static and dynamic stability of dielectric  
566 elastomer fiber composites. *Materials Today: Proceedings*, 44, 2043–7.
- 567 Shmuel, G. (2013). Electrostatically tunable band gaps in finitely extensible dielectric elastomer  
568 fiber composites. *International Journal of Solids and Structures*, 50, 680–6.
- 569 Shmuel, G., & Band, R. (2016). Universality of the frequency spectrum of laminates. *J. Mech. Phys.  
570 Solids*, 92, 127–36. doi:<http://dx.doi.org/10.1016/j.jmps.2016.04.001>.
- 571 Shmuel, G., & Debotton, G. (2012). Band-gaps in electrostatically controlled dielectric laminates  
572 subjected to incremental shear motions. *J. Mech. Phys. Solids*, 60, 1970–81. doi:10.1016/j.jmps.2012.05.006.
- 574 Shmuel, G., & Pernas-Salomón, R. (2016). Manipulating motions of elastomer films by  
575 electrostatically-controlled aperiodicity. *Smart Materials and Structures*, 25, 125012.
- 576 Sigmund, O., & Maute, K. (2013). Topology optimization approaches. *Structural and  
577 Multidisciplinary Optimization*, 48, 1031–55.
- 578 Sigmund, O., & Søndergaard Jensen, J. (2003). Systematic design of phononic band-gap materials  
579 and structures by topology optimization. *Philosophical Transactions of the Royal Society of  
580 London. Series A: Mathematical, Physical and Engineering Sciences*, 361, 1001–19.
- 581 Su, Y., Chen, W., & Destrade, M. (2019). Tuning the pull-in instability of soft dielectric  
582 elastomers through loading protocols. *International Journal of Non-Linear Mechanics*,  
583 113, 62–6. URL: [https://www.sciencedirect.com/science/article/pii/  
584 S0020746218306863](https://www.sciencedirect.com/science/article/pii/S0020746218306863). doi:[https://doi.org/10.1016/j.ijnonlinmec.2019.  
585 03.008](https://doi.org/10.1016/j.ijnonlinmec.2019.03.008).
- 586 Su, Y., Wu, B., Chen, W., & Lü, C. (2018). Optimizing parameters to achieve giant deformation  
587 of an incompressible dielectric elastomeric plate. *Extreme Mechanics Letters*, 22, 60–8.  
588 doi:<https://doi.org/10.1016/j.eml.2018.05.004>.
- 589 Suo, Z., Zhao, X., & Greene, W. H. (2008). A nonlinear field theory of deformable dielectrics.  
590 *Journal of the Mechanics and Physics of Solids*, 56, 467–86.
- 591 Svanberg, K. (1987). The method of moving asymptotes—a new method for structural  
592 optimization. *International journal for numerical methods in engineering*, 24, 359–73.

- 593 Vatanabe, S. L., Paulino, G. H., & Silva, E. C. (2014). Maximizing phononic band gaps in  
594 piezocomposite materials by means of topology optimization. *The Journal of the Acoustical*  
595 *Society of America*, *136*, 494–501.
- 596 Wang, Y.-F., Wang, Y.-Z., Wu, B., Chen, W., & Wang, Y.-S. (2020). Tunable and active phononic  
597 crystals and metamaterials. *Applied Mechanics Reviews*, *72*.
- 598 Xie, L., Xia, B., Liu, J., Huang, G., & Lei, J. (2017). An improved fast plane wave expansion  
599 method for topology optimization of phononic crystals. *International Journal of Mechanical*  
600 *Science*, *120*, 171–81. doi:[http://dx.doi.org/10.1016/j.ijmecsci.2016.11.](http://dx.doi.org/10.1016/j.ijmecsci.2016.11.023)  
601 023.
- 602 Yi, G., Shin, Y. C., Yoon, H., Jo, S.-H., & Youn, B. D. (2019). Topology optimization for phononic  
603 band gap maximization considering a target driving frequency. *JMST Advances*, *1*, 153–9.
- 604 Yi, G., & Youn, B. D. (2016). A comprehensive survey on topology optimization of phononic  
605 crystals. *Structural and Multidisciplinary Optimization*, *54*, 1315–44.
- 606 Zhang, X., Xing, J., Liu, P., Luo, Y., & Kang, Z. (2021). Realization of full and directional band  
607 gap design by non-gradient topology optimization in acoustic metamaterials. *Extreme Mechanics*  
608 *Letters*, *42*, 101126.
- 609 Zhao, X., Hong, W., & Suo, Z. (2007). Electromechanical hysteresis and coexistent states in  
610 dielectric elastomers. *Physical review B*, *76*, 134113.
- 611 Zhu, F., Wu, B., Destrade, M., & Chen, W. (2020). Electrostatically tunable  
612 axisymmetric vibrations of soft electro-active tubes. *Journal of Sound and Vibration*,  
613 *483*, 115467. URL: [https://www.sciencedirect.com/science/article/pii/](https://www.sciencedirect.com/science/article/pii/S0022460X20302996)  
614 [S0022460X20302996](https://www.sciencedirect.com/science/article/pii/S0022460X20302996). doi:<https://doi.org/10.1016/j.jsv.2020.115467>.
- 615 Ziser, Y., & Shmuel, G. (2017). Experimental slowing of flexural waves in dielectric elastomer  
616 films by voltage. *Mech. Res. Commun.*, *85*, 64–8. URL: [http://www.sciencedirect.](http://www.sciencedirect.com/science/article/pii/S0093641317302197)  
617 [com/science/article/pii/S0093641317302197](http://www.sciencedirect.com/science/article/pii/S0093641317302197). doi:[https://doi.org/10.](https://doi.org/10.1016/j.mechrescom.2017.08.005)  
618 [1016/j.mechrescom.2017.08.005](https://doi.org/10.1016/j.mechrescom.2017.08.005).